See related commentary on pg 567

Spatial and Single-Cell Transcriptomics Reveal Keratinocytes as Key Players in Vulvar Lichen Sclerosus Pathogenesis

Peng Sun[1,2,8], Christina N. Kraus[2,8], Wei Zhao[3], Jiahui Xu[1], Susie Suh[2], Quy Nguyen[1], Yunlong Jia[4], Arjun Nair[1], Melanie Oakes[1], Roberto Tinoco[5], Jessica Shiu[1], Bryan Sun[1,2], Ashley Elsensohn[6,7], Scott X. Atwood[2,4], Qing Nie[3,4] and Xing Dai[1,2]

Journal of Investigative Dermatology (2026) **146,** 678–698; doi:10.1016/j.jid.2025.08.022

Vulvar diseases are a neglected area of women's health, profoundly affecting patients' QOL. Lichen sclerosus is a chronic inflammatory vulvar skin disorder leading to severe itching, pain, scarring, and an increased risk of malignancy. Despite this burden, the molecular pathogenesis of vulvar lichen sclerosus is not well-understood, limiting treatment options. In this study, we analyze lesional, nonlesional, and healthy vulvar skin using technologies including spatial and single-cell transcriptomics. Our findings identify unifying molecular changes across multiple cell types in lesional vulvar lichen sclerosus skin, including keratinocyte stress response, necroptosis, and basal/stem cell depletion. Chronic T-cell activation, enhanced cytotoxicity, aberrant cell-cell communication, and elevated IFN-γ/JAK/signal transducer and activator of transcription signaling were also observed. Functional studies suggest keratinocytes' dual role as both targets of microenvironmental signaling (eg, IFN-γ) and sources of inflammatory alarmins (eg, S100A8/9). This work reveals keratinocytes as central players in vulvar lichen sclerosus pathogenesis and identifies potential biomarkers and therapeutic targets for future research.

Keywords: Epidermal keratinocytes, IFN-g/JAK/STAT, Single-cell RNA-sequencing, T cell cytotoxicity, Vulvar lichen sclerosus

INTRODUCTION

Lichen sclerosus (LS) is a chronic inflammatory skin disease that disproportionately affects women (female:male ratio of 6:1–10:1), with vulvar skin being the most common site of involvement (Kreuter et al, 2013). Vulvar LS (VLS) carries a significant disease burden and societal stigma, often resulting in irreversible scarring, infection, sexual dysfunction, genitourinary complications, chronic itch, and pain (Lee et al, 2015; Vittrup et al, 2022; Wijaya et al, 2021). VLS is also associated with malignant transformation to squamous cell carcinoma in approximately 5% of cases (Lee et al, 2015). Although the true prevalence is unknown (Melnick et al, 2020), studies estimate that VLS affects about 1.7% of patients in gynecology clinics (Goldstein et al, 2005). There are no curative or Food and Drug Administration–approved therapies for VLS, and patients require lifelong management with ultrapotent topical corticosteroids to prevent progression and complications such as squamous cell carcinoma and scarring (Lee et al, 2015).

Despite its impact, the pathogenesis of VLS remains poorly understood, with the lack of a standardized staging system further complicating disease study. Although some evidence supports LS as an autoimmune condition, this classification remains controversial (Farrell et al, 1999; Tran et al, 2019). Others argue that LS, particularly in males, is caused by external stressors such as urine (Bunker, 2012). Histologically, VLS is characterized by a lichenoid tissue reaction with epidermal alterations and dermal sclerosis or fibrosis (Day et al, 2023; Weyers, 2015). Infiltration of $CD4^+$, $CD8^+$, and regulatory T cells near the dermoepidermal junction has been reported (Bleeker et al, 2016; Jones et al, 2008; Tran et al, 2019). Chemokine receptor expression patterns (eg, CXCR3 and CCR5) suggest a T helper 1–skewed immune response (Khan Mohammad Beigi, 2022; Loetscher et al,

[1]Department of Biological Chemistry, School of Medicine, University of California, Irvine, Irvine, California, USA; [2]Department of Dermatology, School of Medicine, University of California, Irvine, Irvine, California, USA; [3]Department of Mathematics, University of California, Irvine, Irvine, California, USA; [4]Department of Developmental and Cell Biology, University of California, Irvine, Irvine, California, USA; [5]Department of Molecular Biology and Biochemistry, University of California, Irvine, Irvine, California, USA; [6]Department of Dermatology, Loma Linda University, Loma Linda, California, USA; and [7]Department of Pathology, Loma Linda University, Loma Linda, California, USA

[8]These authors contributed equally to this work.

Correspondence: Christina N. Kraus, Department of Dermatology, School of Medicine, University of California, Irvine, Falling Leaves Medical Innovation Building, 847 Health Sciences Road, Irvine, California 92617, USA. E-mail: ckraus@hs.uci.edu and Xing Dai, Department of Biological Chemistry, School of Medicine, University of California, Irvine, Falling Leaves Medical Innovation Building, 847 Health Sciences Road, Irvine, California 92617, USA. E-mail: xdai@uci.edu

Abbreviations: BS, basal cell; BSC, basal stem cell; cycTC, cycling T cell; DC, dendritic cell; DEG, differentially expressed gene; FFPE, formalin-fixed paraffin-embedded; GC, granular cell; GO, gene ontology; HC, healthy control; K, keratin; LE, lesional; LS, lichen sclerosus; MHC, major histocompatibility complex; NL, nonlesional; p-STAT1, phosphorylated signal transducer and activator of transcription 1; ROI, region of interest; SC, spinous cell; scRNA-seq, single-cell RNA sequencing; siRNA, small interfering RNA; SMA, smooth muscle actin; STAT, signal transducer and activator of transcription; VLS, vulvar lichen sclerosus

Received 11 June 2025; revised 30 July 2025; accepted 1 August 2025; accepted manuscript published online 29 August 2025; corrected proof published online 1 October 2025

1998), although T helper 2 cytokine expression has also been shown (Pilatz et al, 2013). Additional findings, such as autoantibodies against extracellular matrix protein 1 (Terlou et al, 2012), increased synthesis of collagen I and III (De Luca et al, 2023; Zhao et al, 2018), and oxidative stress markers (Paulis and Berardesca, 2019), hint at a complex interplay between immune activation and tissue remodeling. However, most VLS studies to date have been limited in scope, relying on tissue bulk RNA sequencing (Wang et al, 2022) or analysis of a small number of markers, leaving the cellular and molecular mechanisms driving disease progression largely unexplored.

Spatial transcriptomics and single-cell RNA sequencing (scRNA-seq) have transformed our ability to dissect complex inflammatory skin diseases by providing cell type– and state-specific molecular insights into disease pathogenesis. In this study, we apply these techniques to compare lesional (LE) and non-LE (NL) vulvar skin from patients with VLS. Our findings identify gene expression changes across multiple cell types in LE compared with those in NL skin and suggest a central role for keratinocyte dysfunction in VLS—an aspect of pathogenesis that has been largely unexplored. By combining cell- and organ-culture experiments with cell–cell signaling inference, we find that keratinocyte-originated molecular perturbations partially recapitulate VLS-associated changes and identify keratinocytes as potential signal senders and receivers in the VLS skin microenvironment. Finally, we provide evidence for the aberrant activation of IFN-γ/JAK/signal transducer and activator of transcription (STAT) signaling in VLS lesions, linking this pathway activity to keratinocyte stress response and necroptosis—both key features of the LE skin. Overall, our study provides, to our knowledge, the most comprehensive molecular and cellular characterization of VLS to date, revealing keratinocytes as key players in disease pathogenesis.

RESULTS

LE skin from patients with VLS exhibits interpatient heterogeneity, with epidermal alterations, including basal/stem cell reduction, aberrant differentiation, and both necroptotic and apoptotic cell death

To enhance our morphological and biochemical understanding of VLS, we conducted histologic analysis coupled with immunostaining on clinically archived formalin-fixed paraffin-embedded (FFPE) human vulvar skin specimens. We compared LE samples from patients with VLS to NL samples from the same patients and to samples from healthy control (HC) vulvar skin without VLS. Deidentified patient samples by assay are included in Supplementary Table S1. As reported by others (Athota and Kolalapudi, 2021), we observed remarkable intra and interpatient heterogeneity in the histological features of VLS lesions, with predominantly inflammatory or sclerotic subtypes, each showing varying degrees of epidermal changes (Figure 1a and Supplementary Table S1). Sclerotic changes, characterized by marked dermal collagen homogenization, appeared to start in the papillary dermis and spread to the reticular dermis, leaving behind a largely acellular extracellular matrix (Figure 1a4 and a4′). Immunostaining with the fibroblast intermediate filament protein vimentin and the pericyte/smooth muscle cell marker smooth muscle actin (SMA) did not reveal clear alterations in the dermis of nonsclerotic LE relative to that of NL skin (Supplementary Figure S1a). Consistent with the varying degrees of lichenoid inflammation, immunofluorescence using CD45 (a pan-immune cell marker) and CD3 (a T-cell marker) revealed differing levels of total immune and T-cell abundance in both the epidermis and dermis (Figure 1b and Supplementary Figure S1b). In addition, immune cells were found in cellular aggregates deep within the reticular dermis of fully sclerotic LE skin (Supplementary Figure S1b). Interestingly, although immune cells were also detected in NL and HC skin, they appeared more elongated or dendritic, whereas those in LE skin had a more rounded shape (Figure 1b and Supplementary Figure S1b and c), possibly reflecting enrichment of different types of immune cells in HC/NL versus LE skin.

The histological abnormalities of LE skin epidermis included hyperkeratosis, columns of parakeratosis, hypergranulosis, acantholysis of keratinocytes adjacent to the basal layer, and effacement of the epidermis (loss of rete ridges) (Figure 1a and Supplementary Table S1). In addition, there were alterations in the dermoepidermal junction with a lichenoid interface pattern or subepidermal separation. Immunostaining with keratinocyte differentiation markers keratin K5/K14/K15 (basal), K10 (spinous), and loricrin (granular) revealed variable staining pattern changes in LE skin (Figure 1c and d). Nearly all samples showed comparable K14 expression levels between NL and LE skin, except for 1 LE skin sample, which exhibited reduced K5/K14 signals in basal cells (BCs) but elevated staining at the skin surface (Figure 1c and Supplementary Figure S1d). Patchy K10 expression and/or persistent K5 signals were observed in the suprabasal compartment of some LE samples (Figure 1c). Loricrin expression varied considerably, with some LE samples showing strong staining, whereas others showed little to no expression (Figure 1c). K15, a keratin protein typically enriched in epidermal basal stem cells (BSCs) (Bose et al, 2013), was reduced or lost in 5 of the 7 LE samples examined (Figure 1d), suggesting a potential reduction of BSCs in VLS.

Ki-67 immunostaining was not reduced in the samples of LE skin that we evaluated, despite the presence of epidermal atrophy (Supplementary Figure S1e). In addition, analysis of the epithelial cell–adhesion marker E-cadherin revealed disrupted membrane staining in some suprabasal cells of the LE skin (Supplementary Figure S1e and f). A subset of LE suprabasal cells lacked visible DAPI staining, suggesting nuclear loss (Supplementary Figure S1f). To determine whether this was due to cell death, we immunostained NL and LE skin for cleaved caspase 3, a marker of apoptosis (Porter and Jänicke, 1999), and phosphorylated MLKL, a marker of necroptosis (Sun et al, 2012). Apoptotic cells were identified in 3 of the 7 LE samples, with staining observed in basal and suprabasal keratinocytes but absent in NL skin (Figure 1d and e). Necroptotic cells were detected in 5 of the 7 LE samples, primarily affecting basal keratinocytes and the adjacent suprabasal cells, but were not present in NL controls (Figure 1e and f). Although apoptosis and necroptosis have traditionally been considered mutually exclusive at a molecular level, both processes coexisted in some LE samples,

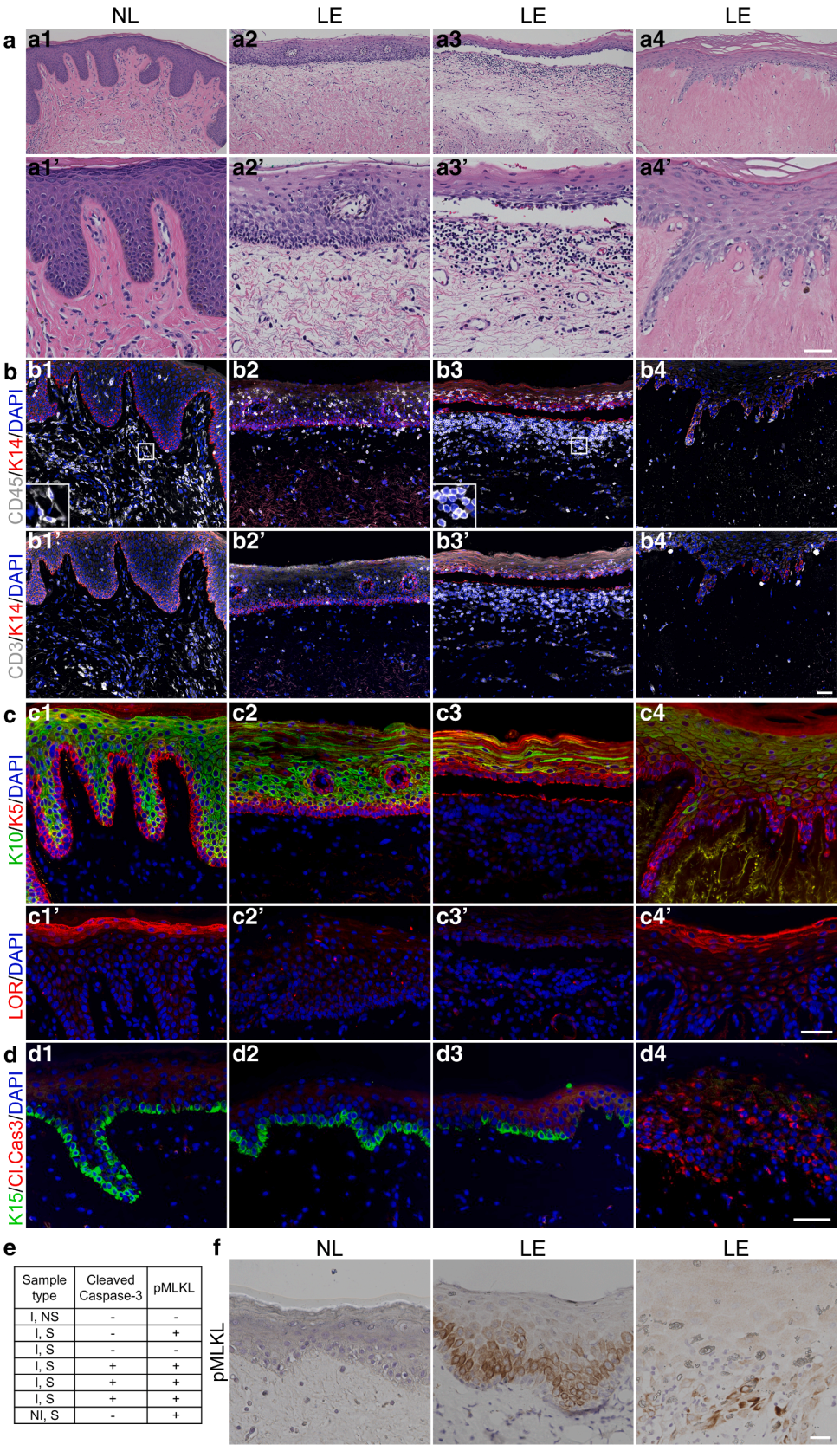

Sample type	Cleaved Caspase-3	pMLKL
I, NS	-	-
I, S	-	+
I, S	-	-
I, S	+	+
I, S	+	+
I, S	+	+
NI, S	-	+

Figure 1. Histological hallmarks, immune infiltration, epidermal changes, and cell death in LE skin of patients with VLS. (**a**) Representative H&E staining images of LE skin from patients with VLS (a2–a4, a2′–a4′), with various levels of inflammation and sclerosis compared with NL (a1, a1′) vulvar skin. A2 and A3 show atrophic epidermis and loss of rete ridges, with dermal edema and lichenoid infiltrate. A4 shows a fully sclerotic lesion with dermal collagen homogenization. Bar = 160 μm in top panels and 50 μm in bottom panels. (**b**–**d**) Immunofluorescence of NL and LE skin with the indicated antibodies. DAPI stains the nuclei. Insets in b1 and b3 show higher magnification of the boxed areas. Bar = 50 μm in **b** and **c**, 25 μm in **d**, and 16 μm for insets. (**e**) Summary of cell death analysis for **d** and **f**, with **f** showing representative immunohistochemical images for pMLKL in NL and LE samples. Samples were categorized per histological changes: I denotes inflammatory, S denotes sclerotic, NI denotes noninflammatory, and NS denotes nonsclerotic. Bar = 25 μm. K14, keratin 14; K5, keratin 5; LE, lesional; LOR, loricrin; NL, nonlesional; pMLKL, phosphorylated MLKL; VLS, vulvar lichen sclerosus.

although not necessarily within the same cells, and were observed in both inflammatory and sclerotic subtypes (Figure 1d–f).

Collectively, these findings confirm previous reports of immune infiltration and epidermal–dermal changes in VLS skin, highlighting aberrant differentiation, disrupted spatial organization, and both apoptotic and necroptotic cell death in the LE epidermis.

GeoMx spatial transcriptomics reveals a keratinocyte stress response in LE skin epidermis of patients with VLS

To elucidate gene expression differences in epidermal and dermal compartments of VLS LE and control skin, we analyzed clinically archived FFPE tissue specimens using a spatial transcriptomics platform, the GeoMx Digital Spatial Profiler (NanoString) (Merritt et al, 2020). We performed 2 independent runs of 7 FFPE samples: 2 LE and 1 NL samples from a patient with VLS, 1 LE sample and 1 NL sample from a second patient with VLS, an unmatched LE sample from a third patient with VLS, and an NL sample obtained from benign excision. We used fluorescent markers for pan-cytokeratin and SMA to select the regions of interest (ROIs), with 151 ROIs yielding quality sequencing information (Figure 2a). These ROIs fell within 7 major spatial compartments divided into epidermal and dermal regions: basal (both inter-ridge and rete ridge), inter-ridge suprabasal, rete-ridge suprabasal, papillary dermis (further segmented into SMA^+ and SMA^-), and reticular dermis (SMA^+ and SMA^-).

Transcriptome profiles from LE and NL skin were integrated, and uniform manifold approximation and projection analysis of all ROIs revealed 2 major clusters on the basis of epidermal or dermal gene expression (Figure 2b). Top markers of the spatial regions were consistent with their identity designation (Figure 2c). Within the epidermal cluster, rete-ridge suprabasal cells predominantly occupied intermediate positions between basal and suprabasal cells, which were segregated at opposite ends of the cluster (Figure 2b). This suggests that they represent a transitional state in the basal-to-suprabasal spectrum that is frequently lost in LE skin. Within the dermal cluster, papillary and reticular dermal cells were not clearly segregated, although a subset of SMA^+ dermal cells appeared to form a distinct subcluster (Figure 2b, top right).

Using Seurat for uniform manifold approximation and projection analysis, we identified 4 major cell clusters: 2 epidermal and 2 dermal (Figure 2b, bottom right). The 2 epidermal clusters were designated basal and suprabasal on the basis of known cell-type markers (Figure 2d and e and Supplementary Table S2). Dermal clusters were designated FB1 and FB2, with FB1 being more enriched with pan-fibroblast genes (eg, *PDGFRA*, *COL1A1*) and FB2 more with SMA^+ cell-associated genes (eg, *ACTA2*, *RGS5*) (Figure 2d and e). FB1 and FB2 were also differentially contaminated with keratinocyte-derived transcripts. Major differences between LE and NL epidermis included increased expression of terminal-differentiation gene *IVL*, stress-associated keratin genes (*K6A*, *K16*, *K17*) (Cohen et al, 2024; Zhang et al, 2019), tissue injury–associated alarmins (*S100A8*, *S100A9*) (Zhang et al, 2019), *KLK10* (serine protease that is dysregulated in psoriasis) (Komatsu et al, 2007), and *ANXA1* (annexin A1) as well as decreased expression of *CCL27* (chemokine known to be decreased in multiple inflammatory skin diseases) (Davila et al, 2022) in LE skin (Figure 2f and Supplementary Table S2). Molecular alterations in fibroblast-enriched dermal populations were less pronounced. *CILP*, an antagonist of TGF-β1 and IGF1 (Mori et al, 2006) and *APCDD1*, a Wnt signaling inhibitor (Shimomura et al, 2010), were both decreased in LE skin (Figure 2f). Interestingly, IgG gene expression was seen in the dermis of some LE samples but not in control counterparts (Supplementary Figure S2a), suggesting that B cells might be transiently present in the LE skin.

As proof-of-principle validation of GeoMx-generated findings, RNAScope analysis confirmed that although stress keratin genes *K6* and *K16* were expressed in the basal layer of NL epidermis, their expression was elevated or expanded in LE skin to varying extents (Figure 2g and Supplementary Figure S2b). Collectively, these findings provide evidence for tissue injury and a keratinocyte stress response in VLS skin lesions.

scRNA-seq analysis corroborates and expands on epidermal stem/progenitor cell depletion, premature terminal differentiation, and stress response activation in LE skin

To systemically evaluate the cellular and molecular alterations in VLS at a single-cell level, we performed scRNA-seq on patient-matched LE and NL vulvar skin samples collected from punch biopsies of 5 patients with biopsy-proven VLS (Supplementary Table S3), using the 10x Genomics Chromium platform (Figure 3a). One pair of samples was excluded from analysis owing to low cell viability in the LE sample. Notably, the participant from whom this pair of samples was obtained was the oldest and had the longest self-reported disease history, with corresponding histology showing a sclerotic phenotype (Supplementary Figure S3a and Supplementary Table S3). Sequencing metrics, including the number of captured cells per sample and average reads per cell, are summarized in Supplementary Figure S3b. After integrating the remaining 8 samples using Seurat, correcting for batch effects, filtering low-quality cells, and removing cell doublets (Materials and Methods), we obtained sequences from a total of 50,545 cells, with 26,938 cells from NL skin (NL1: 7385; NL2: 12,190; NL3: 2893; NL4: 4470) and 23,607 cells from LE skin (LE1: 5744, LE2: 9452, LE3: 1606, LE4: 6805). Uniform manifold approximation and projection clustering revealed 6 major cell clusters on the basis of top expressed genes and known cell-type markers (Solé-Boldo et al, 2020; Zou et al, 2021): keratinocytes (eg, *K5*, *K1*), immune cells (*PTPRC*), fibroblasts (*PDGFRA*), smooth muscle/pericytes (*ACTA2*), endothelial cells (*CLDN5*), and melanocytes (*PMEL*) (Figure 3b–d and Supplementary Table S3). All major cell types present in NL samples were also detected in LE samples, with differing relative abundances (Figure 3b and Supplementary Figure S3c).

To investigate keratinocyte differences between LE and NL skin, we isolated all keratinocyte clusters from the integrated dataset, resulting in a total of 30,604 keratinocytes: 15,061 from NL skin and 15,543 from LE skin. We identified 6 distinct keratinocyte subsets according to their top markers: 3 basal subtypes (BSCs, cycling BCs, and bulk BCs) as well as 3

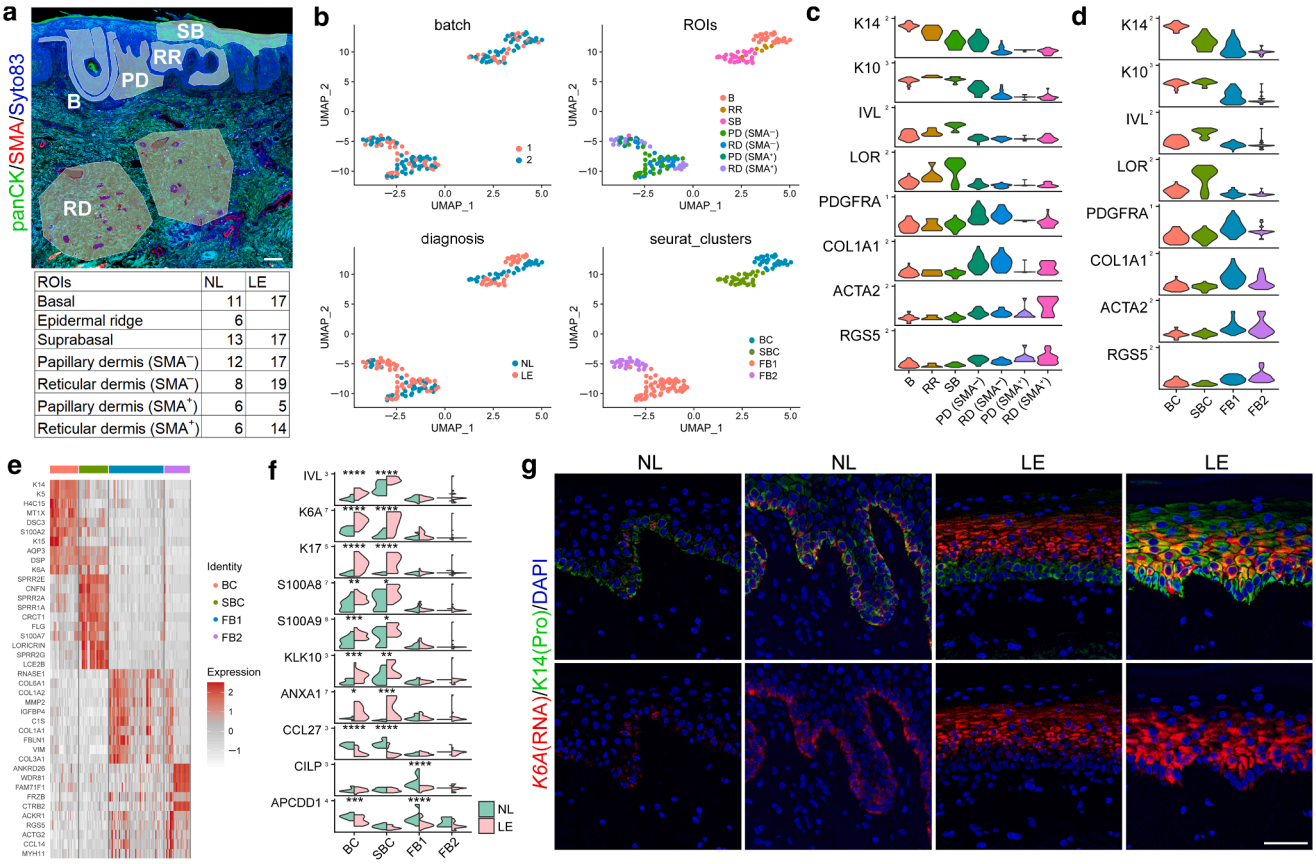

Figure 2. GeoMx analysis reveals gene expression differences between NL and LE skin in epidermal and dermal compartments. (**a**) Representative image showing ROI selection (top) and number of ROSs for each compartment (bottom). B denotes basal, RR denotes rete-ridge basal, SBC denotes suprabasal, PD denotes papillary dermis, and RD denotes reticular dermis. panCK and SMA were used as morphology markers, and Syto83 stains the nuclei. Bar = 100 μm. (**b**) UMAPs by batch (2 independent runs), epidermal or dermal ROIs, diagnosis (NL vs LE), or unsupervised clustering (bottom right panel). (**c, d**) Violin plots showing the expression of select marker genes in different (**c**) ROIs or (**d**) Seurat clusters (BC denotes basal cells, SBC denotes suprabasal cells, FB1 denotes fibroblast population 1, and FB2 denotes fibroblast population 2). (**e**) Heatmap of top 10 marker genes for each Seurat cluster. (**f**) Split violin plot showing select top genes differentially expressed between NL and LE skin in each Seurat cluster. *$P < .05$, **$P < .01$, ***$P < .005$, and ****$P < .001$. (**g**) RNAScope data showing expanded expression of K6 in LE skin. K14 protein staining marks predominantly the basal layer. Bar = 50 μm. K14, keratin 14; K16, keratin 16; LE, lesional; LOR, loricrin; NL, nonlesional; panCK, pan-cytokeratin; ROI, region of interest; SMA, smooth muscle actin; UMAP, uniform manifold approximation and projection.

differentiating subtypes (spinous cells [SCs] 1 and 2, and granular cells [GC]) (Figure 3e–g). This organization in the vulvar skin is consistent with epidermal compartments observed in human skin from other body regions, such as foreskin and hip skin (Wang et al, 2020; Wiedemann et al, 2023), but with distinctions (Supplementary Figure S3d; Wiedemann et al, 2023). In LE skin, there was a notable increase in the more differentiated keratinocyte subtypes, specifically the SC2 and GC subpopulations (average for NL = 19.3% and for LE = 42.8% for SC2 and average for NL = 7.9% and for LE = 16.5% for GC) (Figure 3h and Supplementary Figure S3d). This was accompanied by a decrease in the basal and early spinous subpopulations (Figure 3h and Supplementary Figure S3d), suggesting depletion of epidermal stem/progenitor and transitional states.

To verify that conclusions derived from the integrated master dataset held true for individual pairs of NL and LE samples before batch correction, we also conducted NL–LE pair-wise aggregation and subclustering analysis. This analysis confirmed a decrease in basal and early spinous keratinocytes and an increase in late differentiating keratinocytes in LE samples, with variable patterns across patient samples and the emergence of aberrant differentiation trajectories in some LE samples (Supplementary Figure S3e–g). These data, along with the observed loss of rete ridges containing basal–suprabasal intermediate states (details provided in GeoMx analysis), suggest that the epidermal phenotype in LE skin involves depletion of stem/progenitor and transitional cells, accompanied by premature terminal differentiation.

To further investigate keratinocyte differentiation abnormalities in LE skin, we employed RNA velocity, a computational method that predicts the future state of individual cells by assessing the relative abundance of spliced and unspliced transcripts in single-cell data (La Manno et al, 2018). Velocity calculations using both linear and nonlinear methods on the integrated scRNA-seq dataset revealed major differences in the differentiation trajectories of keratinocytes between NL and LE samples (Supplementary Figure S3h). Both models

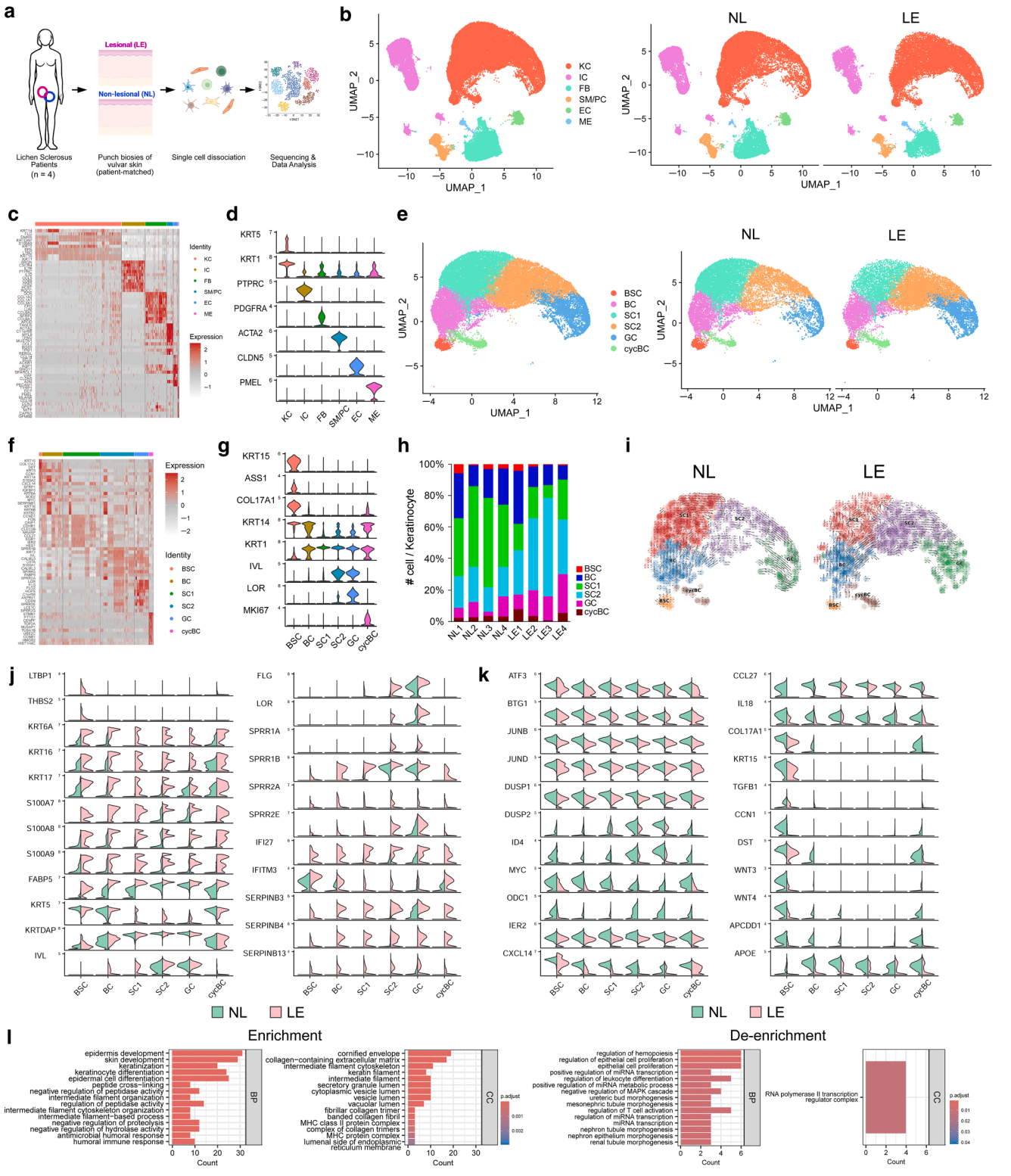

Figure 3. scRNA-seq workflow and overall comparison between NL and LE skin, with subclustering of keratinocytes revealing distinct subclusters and molecular differences. (**a**) Schematic diagram detailing the scRNA-seq workflow. Image was created with BioRender.com. (**b**) UMAP of distinct cell clusters in data integrated from all 8 samples (4 NL, 4 LE) (left) and separated by NL and LE (right). KC denotes keratinocytes, IC denotes immune cells, FB denotes fibroblasts, SM denotes smooth muscle cells, PC denotes pericytes, EC denotes endothelial cells, and ME denotes melanocytes. (**c**) Heatmap with top 10 marker genes for each major cell type. (**d**) Violin plots of select markers for each major cell type. (**e**) UMAP of subtypes of keratinocytes in integrated data (left) and separated into NL and LE (right). (**f**) Heatmap with top 10 marker genes for each subtype of keratinocytes. (**g**) Violin plot of select markers for each subtype of keratinocytes. (**h**) Bar plot showing relative proportions of keratinocyte subclusters for all patient samples (NL and LE). (**i**) Projection of TFvelo velocity fields onto the UMAP space of keratinocytes in NL and LE. (**j, k**) Split violin plots of select genes (**j**) upregulated or (**k**) downregulated in LE keratinocyte subsets compared with those in NL counterparts. (**l**) Diagram showing GO biological process terms enriched (left) and de-enriched (right) in LE keratinocytes compared with those

identified an absence of "backward" transitions from SC to BC and indicated a relative "inertness" of SC2 and GC populations in LE compared with those in NL skin (Supplementary Figure S3h). In addition, we employed a modified velocity analysis method, known as TFvelo (Li et al, 2024), which uses scRNA-seq data on the basis of transcription factor–target relations and incorporates prior knowledge from a transcription factor–target database (on behalf of The ENCODE Project Consortium, 2004). This method provided a more robust projection of epidermal differentiation trajectories, while corroborating the observed differences in SC "reversibility" and GC "inactivity" between NL and LE skin (Figure 3i). These findings suggest reduced plasticity in the early stages and altered differentiation trajectories in the later stages of keratinocyte differentiation within LE skin.

We next identified differentially expressed genes (DEGs) between NL and LE keratinocyte subtypes. Supplementary Table S4 shows the top DEGs upregulated or downregulated in at least 1 keratinocyte subset of LE skin compared with that of its NL counterpart. Some subset-specific changes were detected, such as elevated expression of *LTBP1* and *THBS2* and reduced expression of *K15*, in LE BSCs (Figure 3j and k). Importantly and corroborating the GeoMx data, we observed upregulation of tissue damage/stress-associated genes, including stress keratins (*K6A/B/C*, *K16*, *K17*), alarmins (*S100A7/8/9*), *FABP5*, and *SERPINB3/4/14*, across multiple LE keratinocyte subsets (Figure 3j and k). Variable changes in early epidermal differentiation markers (eg, *K5/14*, *KDAP*, *IVL*) were observed, with notably elevated expression of late differentiation genes (eg, *FLG*, loricrin gene *LOR*, and *SPRR* family members) across multiple keratinocyte subsets in LE samples, supporting the notion of premature epidermal differentiation. Finally, the expressions of *IFI27* and *IFITM3*, 2 IFN-induced genes (Hsieh et al, 2015), were elevated across multiple LE keratinocyte subsets (Figure 3j).

We also identified downregulated DEGs across multiple keratinocyte subsets in LE compared with those in NL skin. These include mitogen-induced early response genes (eg, *ATF3* [Epanchintsev et al, 2020], *BTG1*, *JUNB/D*, *DUSP1/2* [Horita et al, 2010], *ID4* [Junankar et al, 2015], *MYC* [Tullai et al, 2007], *ODC1*, *IER2*, and *CCN1* [Epanchintsev et al, 2020; Horita et al, 2010; Junankar et al, 2015; Kamaid and Giráldez, 2008; Kyjacova et al, 2021; Machado et al, 2021; Tullai et al, 2007]), several chemokine/cytokine genes (*CXCL14*, *CCL27*, *IL18*) (Ihim et al, 2022), and structural and developmental signaling genes (eg, *COL17A1*, *K15*, *TGFB1*, *DST*, and Wnt signaling ligands/inhibitors *WNT3/4* and *APCDD1*) (Figure 3k). Moreover, *APOE*, encoding a fat-binding protein involved in cholesterol/fat metabolism and implicated in skin inflammation (Martins Cardoso et al, 2019), showed reduced expression predominantly in the cycling BC and SC1 subsets (Figure 3k). Gene ontology (GO) analysis of all keratinocytes revealed an enrichment of terms such as "epidermal development," "keratinization," and "keratinocyte differentiation" and de-enrichment of terms such as "regulation of hematopoiesis" and "epithelial cell proliferation" in LE skin compared with those in NL skin (Figure 3l). Collectively, these gene expression changes provide molecular insights into the epidermal perturbations of LE skin, highlighting activation of keratinocyte stress response and alarmin production as well as premature terminal differentiation of epidermal stem/progenitor cells.

Knockdown of *APOE* and *CXCL14* in human keratinocytes partially recapitulates VLS-like epidermal changes, highlighting APOE's role in regulating stress response and necroptosis

To further evaluate the role of keratinocytes in VLS pathogenesis, we investigated the functional impact of select molecular perturbations. Specifically, we focused on 2 genes with reduced expression in LE keratinocytes, as identified by our scRNA-seq data—*APOE* and *CXCL14* (Figure 4a)—because their keratinocyte-intrinsic functions are still largely unknown (Hiebert et al, 2011; Lloyd et al, 2022; Martins Cardoso et al, 2019; Tsujihana et al, 2022). Using RNAScope, we first validated their downregulation in LE epidermis. *APOE* was expressed in both BCs and SCs, and *CXCL14* was expressed more prominently in BCs of NL skin (Figure 4b). Importantly, *APOE* and *CXCL14* expressions were decreased in the suprabasal and basal compartments, respectively, of LE compared with those of NL skin (Figure 4b).

We next conducted small interfering RNA (siRNA)–mediated knockdown experiments in cultured human N/TERT-2G keratinocytes, an immortalized human keratinocyte cell line (Smits et al, 2017). In monolayer N/TERT-2G cultures, siRNA knockdown of *APOE* and *CXCL14* each significantly reduced keratinocyte proliferation (Figure 4c and d). Remarkably, the expression of stress-associated keratin genes *K6/16/17* as well as alarmin genes *S100A8/9* was significantly upregulated by *APOE* deficiency but not *CXCL14* deficiency, per results using 2 independent siRNAs (Figure 4d and Supplementary Figure S4).

To comprehensively define the molecular changes induced by the knockdown of these genes, we performed bulk RNA-sequencing analysis, which confirmed that knockdown of *APOE* but not *CXCL14* led to elevated expression of stress keratin and alarmin genes (Figure 4e). GO analysis revealed "cornification," "epidermal development," "humoral immune response," and "antimicrobial humoral response" as top terms that are enriched with *APOE* knockdown (Figure 4f). However, *CXCL14* knockdown predominantly resulted in downregulation of genes associated with cell cycle progression (Figure 4g). Importantly, genes collectively upregulated by *APOE* and *CXCL14* knockdown accounted for 35% of the upregulated DEGs identified in our scRNA-seq data, including stress keratins, alarmins, serine proteinase inhibitor, and late differentiation genes (Figure 4h). These data underscore the molecular functions of APOE in regulating epidermal stress response, differentiation, and immune response and of CXCL14 in maintaining the proliferative

in NL keratinocytes. BC, basal cell; BSC, basal stem cell; cycBC, cycling basal cell; GC, granular cell; GO, gene ontology; LE, lesional; NL, nonlesional; SC, spinous cell; scRNA-seq, single-cell RNA sequencing; UMAP, uniform manifold approximation and projection.

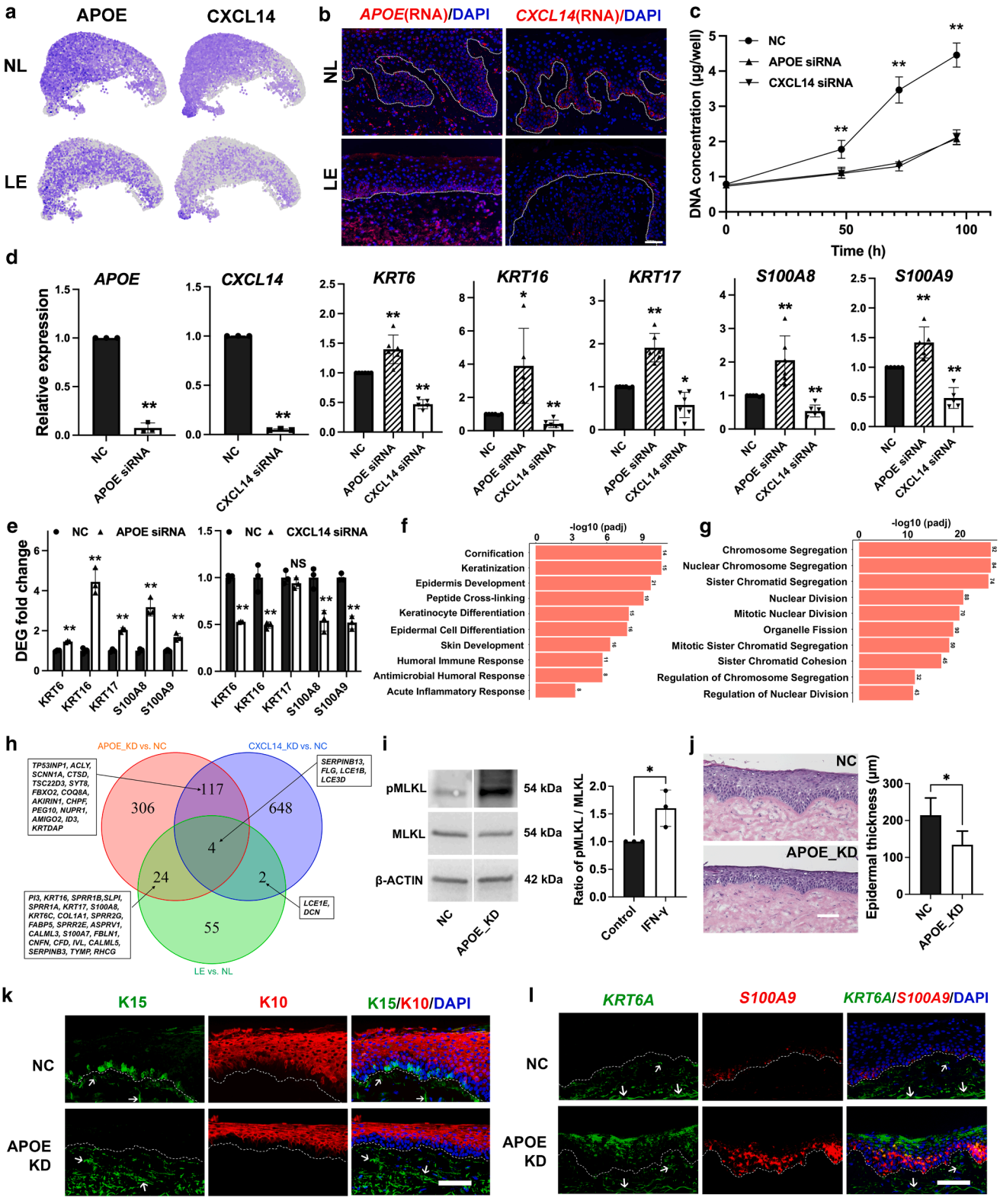

Figure 4. KD of APOE partially recapitulates VLS-like epidermal changes, highlighting its role in regulating keratinocyte stress response and necroptosis. (**a**) Feature plots of APOE and CXCL14 in NL and LE keratinocytes. (**b**) RNAScope data of APOE and CXCL14 transcripts in NL and LE skin. Dotted line indicates basement membrane. Bar = 50 μm. (**c**) Effect of siRNA targeting APOE or CXCL14 on N/TERT-2G keratinocyte proliferation, which was represented by increase in DNA concentration (μg/well) measured 0, 24, 48, and 96 h after siRNA transfection. NC denotes scrambled negative control siRNA. (**d**) RT-qPCR results of the indicated genes analyzed 48 h after siRNA transfection. (**e**) Bulk RNA-sequencing analysis validates the differential expression of the indicated genes. (**f, g**) GO Enrichment analysis of the bulk RNA-sequencing data showing (**f**) top 10 upregulated biological processes upon KD of APOE and (**g**) top 10 downregulated biological processes upon KD of CXCL14. Number above each bar represents the number of genes with significant changes in the APOE or CXCL14 KD group compared with that of the NC group. (**h**) Venn diagram highlighting the overlap of molecular changes across various comparisons: APOE KD versus NC (red), CXCL14 KD versus NC (blue), and LE versus NL in VLS (green). The numbers of overlapping genes are indicated in the diagram, and gene names are listed inside

capacity of keratinocytes. Because necroptosis is a form of inflammatory cell death associated with cellular stress (Tang et al, 2021), we investigated whether *APOE* knockdown impacts keratinocyte necroptosis. Indeed, knockdown led to a significant increase in phosphorylated MLKL/MLKL ratio (Figure 4i), suggesting that APOE plays a protective role in keratinocytes by modulating necroptosis signaling.

Next, we investigated the role of APOE in a more physiologically relevant setting that supports epidermal differentiation, using N/TERT-2G–derived 3-dimensional skin equivalent organotypic cultures. Although epidermal tissue growth and stratification occurred with keratinocytes transfected with negative control siRNA, *APOE* knockdown in keratinocytes resulted in the formation of a thinner epidermis (Figure 4j). Importantly, immunofluorescence and RNAScope analysis revealed reduced expression of K15 and increased expression of stress-associated keratin (*K6A*) and alarmin (*S100A9*) genes, respectively, in the knockdown cultures (Figure 4k and l), recapitulating the findings in LE skin from patients with VLS. These results identify *APOE* as a functional mediator of stress-associated, VLS-like changes in epidermal keratinocytes and implicate the functional importance of keratinocyte-originated perturbations in disease pathogenesis.

Fibroblast alterations in LE skin of patients with VLS are consistent with a proinflammatory and degenerative phenotype, accompanied by reduced collagen production

The known histologic findings of dermal changes in VLS (Weyers, 2015) prompted us to investigate alterations in fibroblasts. We computationally isolated fibroblast clusters from the integrated dataset in Figure 3b yielding 7612 cells for downstream analysis (NL: 4369, LE: 3243). Subclustering revealed 3 fibroblast subpopulations—FB1 (mesenchymal), FB2 (proinflammatory), and FB3 (secretory)—characterized by top markers for each subpopulation and markers reported in previous studies (Deng et al, 2021) (Figure 5a–c). The FB3 cluster exhibited the highest expression of known papillary dermal fibroblast markers, such as *RSPO1*, *APCDD1*, *AXIN2*, *COL6A5*, *COL18A1*, and *COL23A* (Philippeos et al, 2018; Solé-Boldo et al, 2020) (Figure 5c and e and Supplementary Table S5). Variation in the relative frequencies of these fibroblast subpopulations was observed in both NL and LE groups, with a notable trend toward an increased proportion of the proinflammatory (FB2) subpopulation in LE samples (Figure 5d). Pairwise comparison corroborated the relative increase in the FB2 subpopulation and decrease in the FB3 subpopulation in LE samples (Supplementary Figure S5a–c).

Next, we identified DEGs between NL and LE skin within each fibroblast subset (Supplementary Table S5). Compared with other cell types in LE skin, fibroblasts exhibited high levels of transcripts typically restricted to keratinocytes (eg, *K14*), likely owing to contamination with keratinocyte-derived ambient RNAs. These keratinocyte transcripts (Supplementary Table S5) were manually removed from subsequent analysis. Importantly, LE fibroblasts showed upregulation of genes associated with cellular stress and death (eg, *PHLDA2* [Yang et al, 2024], *TMEM45A* [Schmit et al, 2019], *S100A11* [Safronova et al, 2019], *EZR* [Ron et al, 2017], and *TUBA1C* [Sun et al, 2024]), those associated with cell cycle progression (*CCND1*), or those regulating fibrosis and extracellular matrix remodeling (eg, *THY1*, *TAGLN*, *PRSS23*, *TPM1*, *ACTA2*, *MGP*, and *IGFBP6* [Bradbury et al, 2021; El Agha et al, 2017; Hui et al, 2023; LeBleu et al, 2013; Liso et al, 2022; Marangoni et al, 2022; Yu et al, 2008]) (Figure 5e). Among these, *THY1*, *TAGLN*, *TPM1*, and *ACTA2* are known markers of myofibroblasts (Guerrero-Juarez et al, 2019; Koumas et al, 2003), suggesting an "activated" state of LE fibroblasts. *APOE*, previously reported to be expressed in inflammatory fibroblasts (Solé-Boldo et al, 2020), was enriched in the FB2 subpopulation and showed increased expression across all fibroblast subsets in LE samples (Figure 5e). Similarly, *CXCL12*, an FB2-enriched cytokine, was increased in all LE fibroblast subsets (Figure 5e).

DEGs showing significantly decreased expression in LE fibroblasts included (i) developmental signaling genes, such as *PDGFRA*, Wnt agonists (*WNT11*, *RSPO1*) and antagonists (*APCDD1*, *AXIN2*, *NKD2*), *BMP4*, *SPRY1*, and *LEPR*; (ii) early response genes, such as *ID1*, *ID2*, *ID3*, *JUN*, and *CCN1* (Latinkic et al, 1991; Sikder et al, 2003); (iii) endothelial–mesenchymal transitioning–promoting transcription factors *TWIST1/2* (Franco et al, 2011); (iv) oxidative stress–associated genes *KLF9* and *SOD2* (Zucker et al, 2014); and curiously, (v) several neutrophil- or monocyte-attracting chemokines, such as *CXCL1/2/3* and *CCL2* (Supplementary Table S5 and Figure 5e). Of note, multiple structural genes—some of which are papillary fibroblast markers—showed decreased expression, including collagen genes (*COL5A1*, *COL6A1/2*, *COL6A5*, *COL18A1*, *COL23A1*); *TNXB* and *TMEM176B* involved in extracellular matrix organization; *FBLN2*, an extracellular matrix–secreted protein involved in basement membrane zone stability (Ibrahim et al, 2018); and *ELN*, which encodes elastin (Figure 5e).

Pairwise aggregation analysis confirmed the gene expression findings mentioned earlier (Supplementary Figure S5d). GO analysis revealed an enrichment in terms including "regulation of protease activity," "cellular oxidant detoxification," and "regulation of apoptotic pathway" as well as a de-enrichment of terms including "fat cell differentiation," "extracellular matrix organization," and "collagen-containing extracellular matrix" in LE fibroblasts (Figure 5f). Overall, these molecular changes suggest the acquisition of a proinflammatory and degenerative phenotype by LE fibroblasts, at the apparent expense of their developmental, differentiation, and secretory roles. The increased expression of some inflammatory factors, such as *CXCL12*, coupled with the

the rectangles. (**i**) Western blot and band density analysis of the indicated proteins in N/TERT-2G keratinocytes transfected with NC or APOE siRNA for 48 h. (**j**) H&E staining and epidermal thickness in 3D-organotypic human skin equivalents derived from N/TERT-2G keratinocytes transfected with NC or APOE siRNA. (**k**) Immunofluorescence and (**l**) RNAScope of the indicated proteins or transcripts in 3D-organotypic human skin equivalents derived from control or APOE-KD N/TERT-2G keratinocytes. White arrows indicate autofluorescence in the dermis. Bar = 100 μm. $^{**}P < .01$ and $^{*}P < .05$. 3D, 3-dimensional; GO, gene ontology; h, hour; KD, knockdown; LE, lesional; NC, normal control; NL, nonlesional; siRNA, small interfering RNA; VLS, vulvar lichen sclerosus.

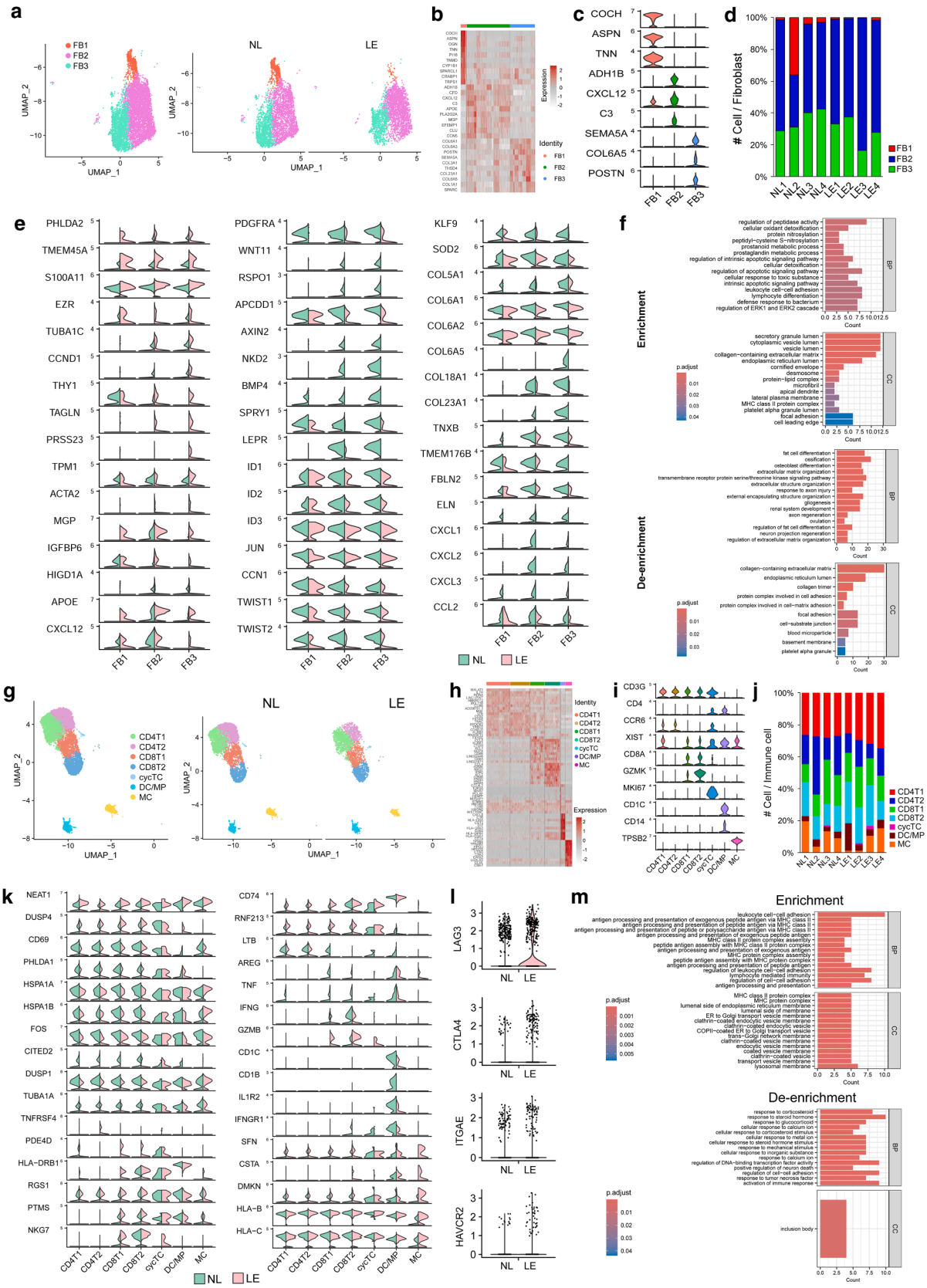

Figure 5. Molecular alterations in LE fibroblasts and immune cells. (**a**) UMAP of subtypes of fibroblasts in integrated data (left) and separated into NL and LE (right). (**b**) Heatmap with top 10 marker genes for each subtype of fibroblasts. (**c**) Violin plot of select markers for each subtype of fibroblasts. (**d**) Bar plot showing relative proportions of fibroblasts subclusters for all patient samples (NL and LE). (**e**) Split violin plots of select DEGs between NL and LE fibroblast subsets. (**f**) Diagram showing GO biological process terms enriched (top) and de-enriched (bottom) in LE fibroblasts compared with that in NL fibroblasts. (**g**) UMAPs of subtypes of immune cells in integrated data (left) and separated into NL and LE (right): CD4T1, CD4+ T-cell 1; CD4T2, CD4+ T-cell 2; CD8T1, CD8+ T-cell 1;

reduced expression of others, such as *CXCL1/2/3*, suggests that fibroblasts may contribute to instructing a chronic inflammatory state rather than an acute one in stable VLS.

Immune responses in VLS are T-cell predominant, with CD8$^+$ T cells exhibiting a cytotoxic and chronically activated phenotype in LE skin

Immune-mediated mechanisms, particularly those associated with a T helper 1–specific IFN-γ–induced phenotype, have been implicated in VLS pathogenesis but with limited evidence (Tran et al, 2019). To comprehensively evaluate immune alterations in VLS, we isolated all immune cell clusters from the integrated dataset, comprising 8314 total cells (NL: 5368, LE: 2946). Downstream subclustering analysis yielded a total of 7 subpopulations: CD4$^+$ T1, CD4$^+$ T2, CD8$^+$ T1, CD8$^+$ T2 (potentially including NK T cells), cycling T cells (cycTCs), dendritic cells (DCs)/macrophages, and mast cells (Figure 5g–i). Variations in the relative frequency of the cell subpopulations were seen in both NL and LE skin, with T cells being the most prominent cell types (>75%) in all samples (Figure 5j). When individual pairs of NL and LE data were aggregated, clustering analysis revealed the presence of additional immune cell types, such as B cells (pair 2) and NK cells (pair 4), which were not uniformly observed across all samples (Supplementary Figure S6a–c). In both integrative and pair-wise analyses, we did not observe a consistent expansion or reduction of any given immune cell type between NL and LE (Figure 5j and Supplementary Figure S6c). These data suggest that an LE-like immune blueprint is already present in NL skin and that the heterogeneous immune response in LE skin likely reflects the spatiotemporal dynamics of disease progression.

Next, we identified DEGs between NL and LE skin in the immune cell clusters (Figure 5k and Supplementary Table S6). Of interest, *NEAT1*, a long-coding RNA that facilitates inflammasome activation in macrophages and promotes T helper 2 cytokine production in CD4$^+$ T cells (Chen et al, 2021; Tibbitt et al, 2019; Zhang et al, 2019), exhibited increased expression in all T-cell subsets and DCs/macrophages of LE compared with those of NL samples (Figure 5k). *DUSP4*, a negative regulator of MAPK pathways in T cells (Horita et al, 2010), demonstrated elevated expression in most T-cell subsets and DCs/macrophages in LE compared with those in NL samples (Figure 5k). Importantly, *CD69*, an early activation marker of immune cells and recently recognized canonical marker of tissue-resident memory T cells (González-Amaro et al, 2013; Ryan et al, 2021; Szabo et al, 2019), was consistently downregulated across nearly all LE immune cell populations (Figure 5k). Reduced expressions of *PHLDA1*, *HSPA1A*, *HSPA1B*, *FOS*, *CITED2*, *DUSP1*, and *TUBA1A* genes with relevance to stress and early response (Khan Mohammad Beigi, 2022) were observed in CD4$^+$ and CD8$^+$ T cells of LE samples (Figure 5k). These data further support the presence of aberrant immune responses in LE skin, which may reflect progression to a later disease stage in the samples analyzed.

DEGs restricted to individual immune cell subsets were observed. For example, *TNFRSF4*, normally expressed in activated CD4$^+$ and CD8$^+$ T cells (Ma et al, 2022), was upregulated in CD4$^+$ T2 cells in most LE samples (Figure 5k). CD8$^+$ T cells of LE samples showed elevated expressions of *PDE4D*, *HLA-DRB1*, *RGS1*, *PTMS*, *CD74*, and *RNF213* (Figure 5k), genes involved in antigen presentation, CD8$^+$ T-cell activation (Kurelic et al, 2021), and dysregulated immune responses (van Drongelen et al, 2021). Particularly notable was the upregulation of cytotoxicity genes (eg, *GZMB* and *NKG7*) in CD8$^+$ T cells and cycTCs of LE samples, whereas the expression of several inflammatory factors (eg, *TNF*, *IFNG*, *LTB*, *AREG*) was surprisingly downregulated (Figure 5k). Furthermore, a targeted analysis revealed elevated expression of known markers of T-cell exhaustion and chronic activation (*LAG3*, *ITGAE*, *CTLA4*, and *HAVCR2*) (Nguyen and Ohashi, 2015; Szabo et al, 2019) in CD8$^+$ T2 cells in LE samples (Figure 5l), suggesting that these cells are in a prolonged activation state.

The DC/macrophage cluster represents a small population that could not be resolved into discrete subsets. Reduced expression of classic DC markers (eg, *CD1C* and *CD1B*) was observed in LE samples (Figure 5k), consistent with the previous report of reduced DC frequency in LS skin dermis (Terlou et al, 2012). Moreover, the LE DC/macrophage cluster showed reduced expression of *IL1R2*, which encodes a decoy receptor for the inflammatory cytokine IL-1 (Martin et al, 2013; Martinez et al, 2006; Rauschmayr et al, 1997) (Figure 5k), suggesting elevated IL-1 signaling in LE skin. Mast cell–specific changes (eg, *SFN*, *CSTA*, *DMKN*, *HLA-B*, and *HLA-C*) in LE skin were also observed (Figure 5k), with elevated expression of major histocompatibility complex (MHC) class I genes (*HLA-B/C*) raising the possibility that mast cells contribute to antigen presentation to CD8$^+$ T cells.

GO analysis of all immune cells revealed enrichment of terms such as "leukocyte cell–cell adhesion" and "antigen processing and presentation through MHC class II" as well as de-enrichment of terms such as "response to corticosteroid," "regulation of DNA-binding transcription factor activity," and "activation of immune response" in LE skin (Figure 5m). Together, our findings underscore the coexistence of an elevated adaptive immune response and aberrant inflammation in VLS, highlighting increased cytotoxicity and the chronic activation of CD8$^+$ T cells in LE skin.

Altered cell–cell signaling in LE skin with elevated JAK/STAT pathway activation in keratinocytes and immune cells

To probe global differences in cell–cell communications in LE compared with those in NL skin, we performed comparative CellChat analysis to study the signaling interaction

CD8T2, CD8+ T-cell 2. (**h**) Heatmap with top 10 marker genes for each subtype of immune cells. (**i**) Violin plot of select markers for each subtype of immune cells. (**j**) Bar plot showing relative proportions of immune cell subclusters for all patient samples (NL and LE). (**k**) Split violin plots of select DEGs between NL and LE immune cell subsets. (**l**) Violin plots of select T-cell exhaustion and chronic activation markers in NL and LE CD8 T2 cells. (**m**) Diagram showing GO biological process terms enriched (top) and de-enriched (bottom) in LE immune cells compared with that in NL immune cells. cycTC, cycling T cell; DC, dendritic cell; DEG, differentially expressed gene; GO, gene ontology; LE, lesional; NL, nonlesional; MC, mast cell; MP, macrophage; UMAP, uniform manifold approximation and projection.

potential among all major cell types (Jin et al, 2021). CellChat infers cell–cell communication networks on the basis of the expression levels of ligands, receptors, and their cofactors. We used a total of 20 cell groups for analysis, including individual subsets of keratinocytes, immune cells, fibroblasts, and other minor cell populations such as melanocytes.

We first examined the total number of potential cell–cell communications and identified the most prominently affected cell types and subtypes. Overall, there was an increased number of potential interactions in NL compared with that in LE skin, among or within the different cell groups (Figure 6a). Putative signaling from all keratinocyte subpopulations to all immune cell subpopulations, excluding mast cells, particularly from BSC and BC to CD8$^+$ T1 and cycTC, showed increased strength in LE skin (Figure 6b). Notably, the CD8$^+$ T1 and cycTC immune subpopulations showed the greatest upregulation as signaling recipients from most cell populations in LE skin compared with those in NL skin (Figure 6b). Melanocytes were the next most upregulated signaling receivers in LE skin, with keratinocytes and melanocytes themselves likely serving as the primary signaling sources (Figure 6b). These findings highlight BSC/BC keratinocytes as among the most activated signaling senders (relative to those in NL skin) and CD8$^+$ T1, cycTCs, and melanocytes as the most activated signaling receivers in the LE skin microenvironment.

To account for potential contamination of LE fibroblasts with keratinocyte-derived transcripts, we subclustered the NL + LE master dataset to computationally remove nearly all "contaminated" fibroblasts and repeated the CellChat analysis. The major conclusions—namely, that CD8$^+$ T1, cycTCs, and melanocytes are the most activated signaling receivers in LE skin—remain unchanged (Supplementary Figure S7a). Interestingly, however, the inflammatory fibroblast subpopulation (FB2) emerged as the strongest signaling sender in LE skin, with keratinocytes, immune cells, FB2 fibroblasts, and pericytes as their primary signaling targets (Supplementary Figure S7a). These findings suggest that FB2 fibroblasts are likely key participants in cell–cell signaling communication in LE skin.

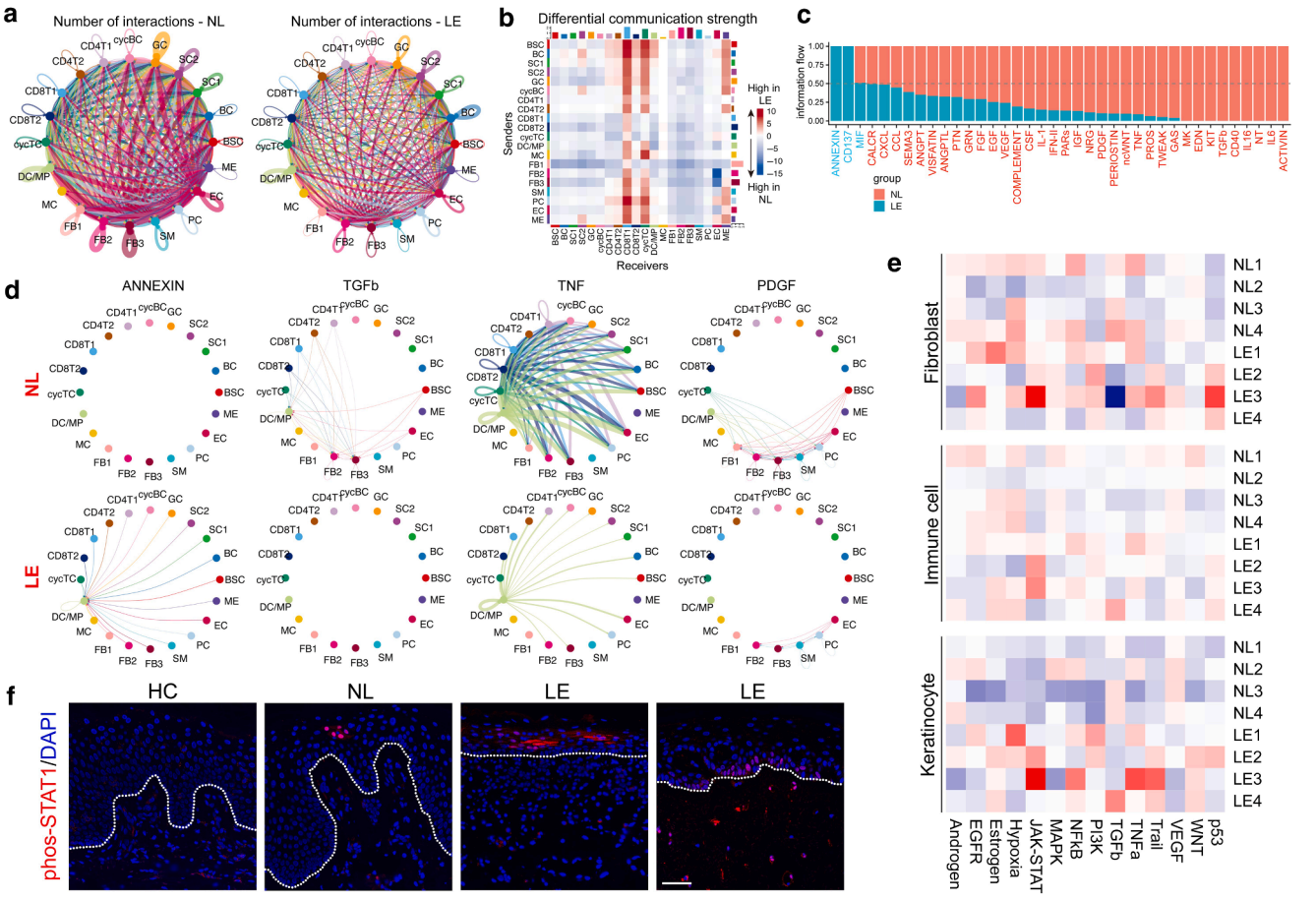

Figure 6. Cell–cell communication and pathway activity changes in LE skin. (**a**) Circle plot (by count) revealing the number of putative ligand–receptor interactions between cell groups for NL and LE; line thickness represents strength of communication. (**b**) Heatmap (by weight) summarizing differential strength of communication in LE compared with that in NL. Red (positive values) and blue (negative values) in the color bar indicate a higher number of predicted interactions in LE and NL skin, respectively. (**c**) Significant signaling pathways were ranked on the basis of their differences of overall information flow, calculated by summarizing all communication probabilities in each inferred network. Those colored red and green are more enriched in NL and LE skin, respectively. (**d**) Chord diagrams of select inferred signaling networks. (**e**) PROGENy analysis of signaling pathway activation in fibroblasts, immune cells, and keratinocytes using scRNA-seq data for all patient samples. (**f**) p-STAT1 immunostaining of HC, NL, and LE skin samples. DAPI stains the nuclei. Dotted line indicates basement membrane. Bar = 50 μm. HC, healthy control; LE, lesional; NL, nonlesional; p-STAT1, phosphorylated signal transducer and activator of transcription 1; scRNA-seq, single-cell RNA sequencing.

Next, we compared the information flow, the sum of communication probabilities among all pairs of cell groups in the inferred network, for specific signaling pathways between LE and NL skin. Considerable variability was observed across patient samples. Of the 41 pathways detected by CellChat, 38 exhibited consistent changes in signaling strengths across both integrated data and at least 2 pairwise comparisons (Figure 6c). Notably, ANNEXIN and CD137 (TNFSF9) pathways showed increased information flow in LE compared with that in NL samples (Figure 6c and d and Supplementary Figure S7b). The increase in immune-modulating ANNEXIN signaling is in part attributed to elevated expression of ANNEXIN 1 (*ANXA1*) in keratinocytes, along with elevated expression of the *FRP1* receptor gene but not *FRP2* in keratinocytes (at low frequency) and immune cells (DCs/macrophages in particular) (Supplementary Figure S7c). Increased CD137 signaling involved $CD8^+$ T2 and cycTCs as signal sender/receiver (Supplementary Figure S7b), consistent with CD137−CD137L being a costimulatory pathway for $CD8^+$ T cells and serving as a critical immune checkpoint with implications for autoimmunity (Otano et al, 2021; Pichler et al, 2023; Wölfl et al, 2008).

Other pathways, such as TGFb, TNF, and PDGF, showed overall reduced information flow in LE skin (Figure 6c and d). TGFb signaling in NL skin involved various senders and 3 primary receivers—FB2, FB3, and DCs/macrophages—with information flow through all signaling routes diminished in LE skin (Figure 6d). TNF signaling was widespread across many cell types in NL but became restricted in LE skin, with DCs/macrophages being the only signaling receiver (Figure 6d). Fibroblasts, smooth muscle cells, and pericytes were the predominant signal receivers of PDGF signaling in NL skin, with decreased overall signaling flow in LE skin (Figure 6d). Collectively, the alterations in the strength and architecture of cell−cell communications in LE skin are suggestive of elevated immune signaling at the expense of developmental signaling.

Although CellChat can predict signaling potential, inferred interactions are hypothetical. To seek more definitive evidence of signaling alterations, we applied PROGENy, a computational pipeline that can infer the activity of 14 signaling pathways using publicly available gene expression data from perturbation experiments (Hu et al, 2015), to our integrated master dataset. Overall, differential signaling activities between LE and NL skin were noted across keratinocyte, fibroblast, and immune cell subsets, with considerable heterogeneity observed among patients and across cell types and subtypes (Figure 6e and Supplementary Figure S7d). In LE keratinocytes compared with their NL counterparts, the phosphoinositide 3-kinase, JAK/STAT, estrogen, TRAIL, and Wnt pathways were elevated, whereas the VEGF pathway was decreased (Figure 6e). LE immune cells exhibited an elevated p53 pathway compared with their NL counterparts, along with increased JAK/STAT activity in most LE samples (Figure 6e). Of note, the LE sample with the least JAK/STAT activation in keratinocytes and no activation in immune cells exhibited the mildest histologic abnormalities, characterized by the absence of dermal sclerosis, retention of epidermal rete ridges, and only minimal immune cell infiltration (Supplementary Figure S7e). LE fibroblasts showed elevation in phosphoinositide 3-kinase and p53 pathways and a decrease in androgen and TGFb pathways (Figure 6e). TGFb signaling, a well-characterized profibrotic pathway, has been reported to be either mildly increased or unchanged in LS skin compared with that in control skin (Akhmetshina et al, 2012), making its decrease in LE fibroblasts particularly intriguing. Of the upregulated pathways, phosphoinositide 3-kinase/protein kinase B signaling plays a role in numerous cellular responses, including proliferation and apoptosis, and exhibits diverse crosstalk mechanisms (Zhang et al, 2013). The JAK/STAT pathway, involved in many vital cellular processes, including cancer and inflammation, is linked to various autoimmune diseases and cancers when dysregulated (Hu et al, 2021). The p53 pathway is activated by various cellular stressors (eg, DNA damage, oxidative stress) to halt the cell cycle and differentiation and to promote apoptosis (Wang et al, 2023). The increased activity of these pathways in LE skin may contribute to aberrant immune responses, disruption of the balance between cell proliferation and differentiation, and excessive cell death, all characteristic features of VLS.

To assess signaling activation in situ, we performed phosphorylated STAT1 (p-STAT1) immunostaining on HC, NL, and LE skin, using a separate cohort of patient samples not included in the scRNA-seq analysis. No specific signals were detected in the epidermis of HC skin. In contrast, sporadic foci of p-STAT1−positive nuclei were detected in the epidermis of NL skin, predominantly in suprabasal keratinocytes near the skin surface (Figure 6f). In LE skin, p-STAT1−positive nuclei were generally more abundant than in NL skin, although with variation among patients and localization in both suprabasal and basal compartments (Figure 6f). p-STAT1−positive signals were also detected in the dermis of HC, NL, and LE skin, but most were not nuclear, except for a subset in LE skin (Figure 6f). These findings reinforce the scRNA-seq findings, identifying epidermal keratinocytes in LE skin as key targets of JAK/STAT activation.

IFN-γ as a potential trigger of keratinocyte stress response and necroptosis in LE skin

IFNs are among the factors (cytokines and GFs) that can activate JAK/STAT signaling (Hu et al, 2021). Given the activation of the IFN-γ/JAK/STAT pathway in other lichenoid inflammatory disorders (eg, lichen planus) (Shao et al, 2019) and the immunohistochemical evidence of increased IFN-γ in VLS (Farrell et al, 2006), we considered the possibility that IFNs may act as signaling stimulators of the JAK/STAT pathway in LE skin. According to our scRNA-seq data, *IFNG* was the most highly expressed ligand in NL/LE skin, whereas *IFNA* expression was undetectable, and *IFNGR1* expression was restricted to DCs/macrophages (and was slightly decreased in LE compared with that in NL skin) (Supplementary Figure S7f and Supplementary Table S5). Immune cells were the predominant *IFNG* expressors, with comparable levels between LE and NL skin (Figure 7a). However, LE keratinocytes; fibroblasts; and, to a lesser extent, melanocytes exhibited higher frequencies of *IFNG*-high expressors than in NL skin (Figure 7a). Among the different immune and stromal cell populations, $CD8^+$ T cells were the major source of IFN-γ, sending signals to various

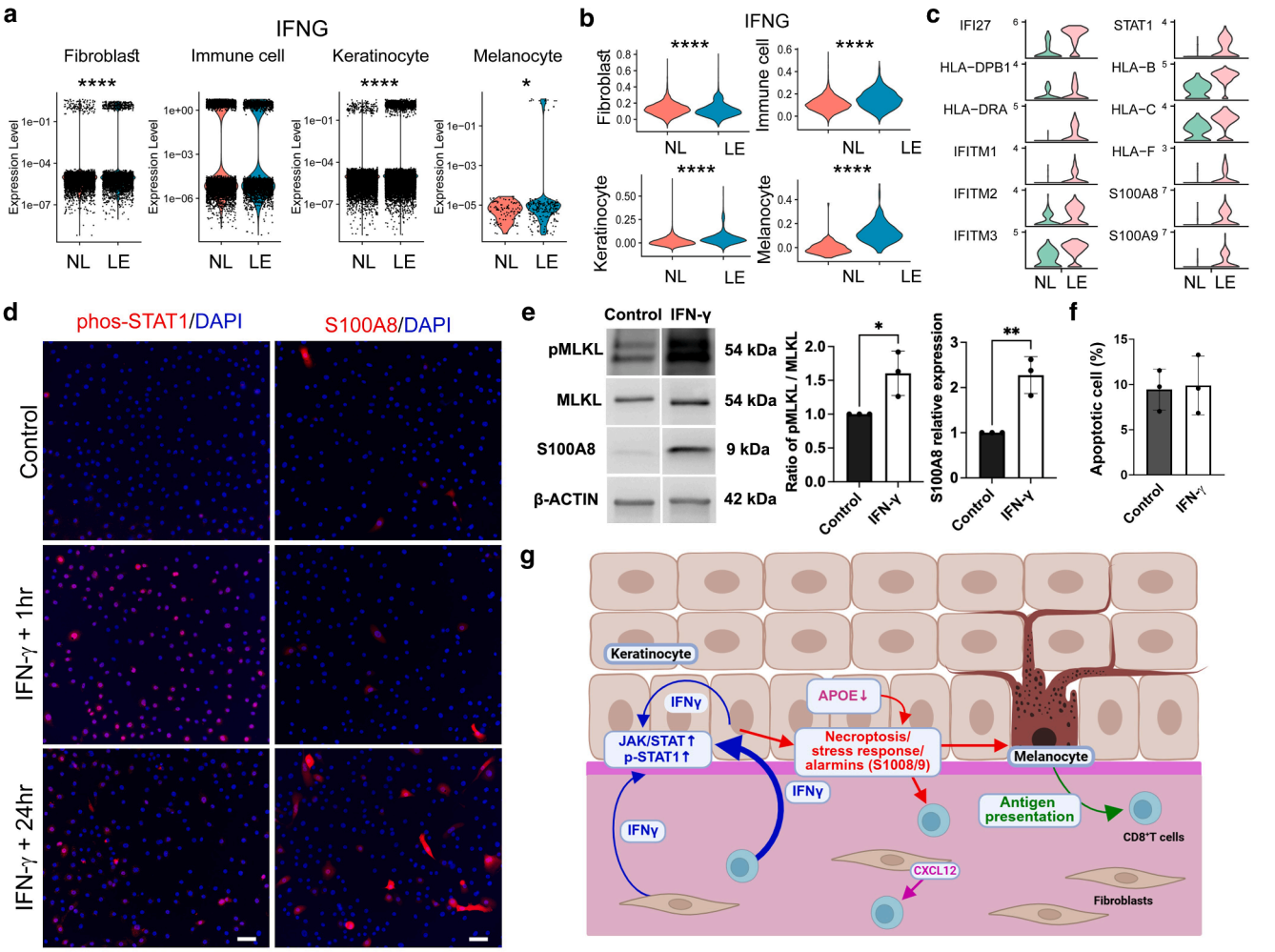

Figure 7. Functional evidence supporting IFN-γ actions in VLS skin and working model for disease pathogenesis. (**a**) Violin plots of IFNG expression by cell type in NL compared with that in LE, visualized by overlaying a jitter plot and transforming data using a log10 scale. *$P < .05$ and ****$P < .001$. (**b**) Gene scoring analysis of the indicated cell types in NL versus LE using MSigDB signatures for HALLMARK_INTERFERON_GAMMA_RESPONSE (IFNG). ****$P < .001$. (**c**) Violin plots of IFN target genes and S100A8/9 in melanocytes of NL and LE skin. (**d**) Immunofluorescence of p-STAT1 or S100A8 in N/TERT-2G human keratinocytes, untreated (control) or treated with IFN-γ for 1 hour (IFN-γ + 1 hour) or 24 hours (IFN-γ + 24 hours). Bar = 50 μm. (**e**) Western blot of pMLKL, total MLKL, and S100A8 protein expression in N/TERT-2G keratinocytes, untreated (control) or treated with IFN-γ for 24 hours. Densitometry quantification shows increased pMLKL/MLKL ratio and S100A8 level in IFN-γ–treated cells. β-Actin was used as loading control. (**f**) Representative flow cytometry plots and quantification of apoptotic cells (PI and FITC Annexin V staining) in control versus IFN-γ–treated N/TERT-2G keratinocytes after 24 hours. (**g**) Working model of VLS pathogenesis. Vertical arrows indicate upregulated or downregulation, whereas the remaining arrows indicate known or potential regulations. LE, lesional; MSigDB, Molecular Signature Database; NL, nonlesional; PI, propidium iodide; pMLKL, phosphorylated MLKL; p-STAT1, phosphorylated signal transducer and activator of transcription 1; VLS, vulvar lichen sclerosus.

keratinocyte subsets and DCs/macrophages (Supplementary Figure S7f).

Next, we compared the IFNG target signature across cell types in NL and LE skin. Molecular Signature Database hallmark analysis revealed elevated IFNG signature expression in LE skin (Figure 7b). Melanocytes showed the most remarkable upregulation, followed by immune cells and keratinocytes. Not only IFN target genes (eg, *IFI27*, *IFITM1*, *IFITM2*, *IFITM3*, *IFI6*) were upregulated, but also the expression of *STAT1* was elevated in melanocytes of most LE samples compared with those of NL samples (Figure 7c). MHC I and II genes are known to be induced by IFN-γ signaling(Giroux et al, 2003; Seliger et al, 2008; Wijdeven et al, 2018), and indeed, several of them (MHC I: *HLA-B*, *HLA-C*, *HLA-F;* MHC II: *HLA-DPB1*, *HLA-DRA*) were upregulated in LE melanocytes (Figure 7c). Intriguingly, MHC I genes were not consistently altered in LE keratinocytes compared with their NL counterparts (Supplementary Figure S3i). These findings highlight melanocytes as a significant target of elevated IFN signaling (Platanias, 2005) as well as their potential role in antigen presentation to both $CD4^+$ (through MHC II) and $CD8^+$ T (through MHC I) cells.

The lack of robust MHC I upregulation in LE keratinocytes, despite IFN/JAK/STAT activation, prompted us to explore whether IFN-γ influences keratinocytes by modulating stress responses and/or cell death. Using N/TERT-2G human keratinocytes, we found that IFN-γ treatment rapidly induced p-STAT1, followed by a marked increase in S100A8 protein levels (Figure 7d and e). In addition, IFN-γ significantly increased phosphorylated MLKL levels without affecting total

MLKL levels (Figure 7e), indicating activation of necroptosis signaling. However, under the same conditions, no detectable increase in apoptotic cell death was observed (Figure 7f). These findings suggest that IFN-γ triggers keratinocyte stress response and activates necroptosis.

DICUSSION

Our study provides an unprecedented overview of VLS-associated cellular and molecular alterations, highlighting a multifactorial etiology for this understudied and clinically impactful disease. Whereas prior studies have suggested immune involvement and dysregulation of fibrotic pathways (Tran et al, 2019), our work points to a central role for keratinocytes in disease pathogenesis. Despite heterogeneity between patients, specific changes in keratinocytes, fibroblasts, immune cells, and melanocytes were observed, with the most striking and uniformly consistent findings being keratinocyte stress response and alarmin production in VLS lesions. Keratinocytes have been implicated in immune-mediated diseases, serving both as sources and targets of inflammatory mediators (Jiang et al, 2020), but their roles in VLS pathogenesis have not been appreciated. Our findings suggest that keratinocytes in VLS skin are not only targets of immune- and nonimmune-derived IFN-γ signaling but also sources of inflammatory alarmins (Figure 7g).

Importantly, our data identify keratinocyte necroptosis as a key feature of VLS and reveal keratinocyte-intrinsic (APOE) and -extrinsic (IFN-γ) factors in VLS lesions that can alter and activate necroptosis signaling in association with stress response (Figure 7g). Necroptosis is a programmed cell death pathway that, distinct from the inflammation-silent apoptosis, is highly inflammatory through the release of alarmins (eg, HMGB1 and S1008/9) rather than classical cytokines such as TNFα (Bai et al, 2021; Schweizer et al, 2021[1]). Necroptotic keratinocytes in psoriasis-like skin are known to release S100A8/9 (Duan et al, 2020), which can be secreted into the extracellular space and promote the induction of autoreactive $CD8^+$ T cells (Srikrishna, 2012). Elevated S100A8/9 levels in lichen planus lesions are linked to enhancement of patient $CD8^+$ T-cell cytotoxicity (de Carvalho et al, 2015). Melanocytes, which typically reside in the basal layer of the epidermis (Lin and Fisher, 2007), are influenced by adhesion and paracrine signaling interactions with keratinocytes (Arnette et al, 2020; Tong et al, 2025), with keratinocyte-derived S100A8/9 known to activate melanocytes and melanoma cells (Shirley et al, 2014). Therefore, necroptotic keratinocytes and elevated levels of S100A8/9 in VLS lesions likely promote a diseased vulvar skin microenvironment in part by activating $CD8^+$ T cells and melanocytes (Figure 7g). Supporting this notion, VLS lesions exhibit elevated annexin A1 signaling, a key factor in Stevens–Johnson syndrome/toxic epidermal necrolysis that promotes keratinocyte necroptosis (Saito et al, 2014). Damage-induced dysregulation in VLS lesions may eventually deplete epidermal stem and progenitor cells as well as the expression of their associated genes (eg, *APOE*, *CXCL14*), leading to tissue atrophy.

[1] Schweizer TA, Shambat SM, Vulin C, Hoeller S, Acevedo C, Huemer M, et al. Blunted Fas signaling favors RIPK1-driven neutrophil necroptosis in critically ill COVID-19 patients. bioRxiv 2021.

We provide evidence of immune alterations in VLS LE skin, characterized by increased $CD8^+$ T-cell cytotoxicity and heightened IFN-γ/JAK/STAT signaling, consistent with a T helper 1–driven disease (De Luca et al, 2023; Farrell et al, 2006; Terlou et al, 2012). Unexpectedly, our findings uncover a gene expression program in VLS LE skin indicative of chronic and advanced immune activation, potentially progressing to T-cell exhaustion. The exact trigger of T-cell activation remains to be determined; however, our scRNA-seq findings suggest that several cell populations—including mast cells and melanocytes but not keratinocytes—may serve as antigen-presenting cells. In addition, the presence of B cells in LE skin of some samples of patients with VLS further supports an antigen-driven response. We propose a working model in which antigen-presenting cells and keratinocyte-derived alarmins act together to initiate and sustain an aberrant immune microenvironment enriched with cytotoxic T cells (Figure 7g). These T cells, in turn, contribute to VLS pathology, at least in part, by inducing keratinocyte necroptosis and stress response.

Our finding of fibroblast changes offers, to our knowledge, previously unreported insights into the clinical scarring changes observed in patients with VLS, which can severely alter vulvar architecture and function (Bradford and Fischer, 2010). In general, the changes are not strongly consistent with typical fibrotic disease, given reduced collagen (eg, *COL6A5*, *COL18A1*) and elastin gene expression as well as reduced TGFβ and PDGF signaling, in the LE skin microenvironment (Beer et al, 1997; He et al, 2020; Iwayama and Olson, 2013; Pilatz et al, 2013; Tran et al, 2019; Trojanowska, 2008). Instead, disease fibroblasts upregulate the expression of CXCL12 that primarily targets T cells and DCs/macrophages (Supplementary Figure S7g) and downregulate the expression of CXCL1/2/3 and CCL2 that predominantly target neutrophils and monocyte/macrophages (Crowl et al, 2022). As such, the inflammatory fibroblasts in VLS are likely distinct from those in other skin diseases, thereby leading to disease-specific patterns of inflammation (Beer et al, 1997; Chiang et al, 2019; Kamata and Tada, 2022; Ma et al, 2023). Although early VLS may involve dermal fibrosis, it is likely that progression to a late, chronic stage results in a degenerative and stressed fibroblast state, as suggested by our scRNA-seq analysis.

Type II IFNs are implicated in autoimmune and inflammatory disorders (Green et al, 2017), with IFN-γ known to enhance T cell-mediated cytotoxicity against keratinocytes in interface-predominant dermatitis, including lichen planus and cutaneous lupus (Lauffer et al, 2018; Shao et al, 2019). Our discovery of elevated IFN-γ/JAK/STAT signaling in VLS LE skin provides critical insight into disease pathogenesis and highlights promising therapeutic strategies. These findings lay the groundwork for clinical trials investigating IFN blockade and JAK/STAT inhibition to clarify their roles in VLS and evaluate their potential as treatment modalities. However, our study is limited in its ability to delineate the precise sequence of pathogenic events and identify the cell(s) of origin of the disease. Future research should prioritize the development of experimental models and innovative approaches to address these challenges.

MATERIALS AND METHODS

Sex as a biological variable

This study focused on individuals assigned female at birth with biopsy-confirmed VLS because the condition under study predominantly affects vulvar skin. As such, only female participants were included in the study. The exclusion of male participants reflects the anatomical specificity of the disease and the need to control for site-specific and sex-dependent variations in skin structure and immune response.

Statistics

Statistical analyses were performed using R (version 2024.04.0+735). For scRNA-seq data, differential gene expression was assessed using the Wilcoxon rank-sum test implemented in the Seurat package. For cell–cell communication inference, significance was assessed using permutation-based methods implemented in CellChat. All *P*-values were two-tailed, and a threshold of $P < .05$ was considered statistically significant unless otherwise specified.

Study design

This study utilized spatial transcriptomics and scRNA-seq to study LE and NL skin in VLS. Histologic specimens and punch skin biopsies were from patients with a diagnosis of biopsy-proven VLS. All samples were deidentified before use in experiments. VLS skin samples were evaluated and obtained by a board-certified dermatologist. Clinically active LS lesions were characterized by the presence of erythema and/or textural change (atrophy, lichenification). Late lesions were characterized clinically by scarring/architectural changes. NL sites were selected as skin adjacent to the site of VLS with the absence of any of the morphologic findings (texture change, erythema, hypopigmentation/depigmentation, scarring) of VLS clinically and under dermoscopy.

Participant enrollment

Five participants were enrolled for scRNA-seq experiments of both LE and NL skin. Participants enrolled had not used topical steroids or another topical immunomodulators in the 2 weeks prior to sample procurement. Patients were not on a biologic or systemic immunomodulator for VLS or another condition. All patients were postmenopausal and were not on topical or systemic hormonal replacement at the time of biopsy. Patients included did not have a diagnosis of a concomitant vulvar dermatosis (eg, lichen planus) or infectious process.

Patient samples for immunohistochemistry, immunofluorescence, GeoMx, and RNAScope

Human skin FFPE samples, obtained for diagnostic purposes from patients with VLS or from benign vulvar excisions in non-VLS patients, were analyzed and subjected to the indicated assays.

Histology, immunostaining, and RNAScope

For paraffin-embedded human vulvar samples, 4-μm sections were stained with H&E using the H&E Stain Kit (Abcam) per the manufacturer's instructions or using the appropriate antibodies after antigen retrieval as previously described (Dragan et al, 2022). Primary antibodies included K5, K10, K14, K15, loricrin, CD3, CD45, SMA, vimentin, Ki-67, E-cadherin, cleaved caspase-3, and phosphorylated MLKL, and fluorescence-conjugated secondary antibodies used included Alexa Fluor 488–conjugated goat anti-mouse, Alexa Fluor 568–conjugated goat anti-rabbi, Cy5-conjugated donkey anti-mouse, Alexa Fluor 647–conjugated donkey antirabbit, and FITC-conjugated donkey antirabbit (information is provided in Supplementary Table S7). Immunohistochemical detection was performed using the Vector ABC (Vector Laboratories, PK-6100) and 3,3′-diaminobenzidine (Dako, K3468) kits according to the manufacturers' instructions.

RNAScope was performed as described (Vu et al, 2022) using the following probes: Hs-K6A, Hs-S100A9, Hs-K16, Hs-APOE, and Hs-CXCL14 (information is provided in Supplementary Table S7). Images were acquired with a Keyence microscope.

Keratinocytes-derived 3-dimensional skin organotypic cultures were freshly frozen in Tissue-Tek O.C.T. Compound (Sakura) and sectioned at 10 μm on Superfrost Plus microscope slides (Thermo Fisher Scientific). Sections were fixed at room temperature for 1 hour with 4% paraformaldehyde (Electron Microscopy Sciences) diluted in 1x PBS (Gibco), followed by H&E staining or immunofluorescence using the indicated primary antibodies in conjunction with Alexa Fluor 488–conjugated goat antimouse and Alexa Fluor 568–conjugated goat antirabbit as secondary antibodies (Supplementary Table S7).

GeoMx spatial transcriptomics

FFPE specimens were sectioned and mounted onto histology-grade glass slides. Slides were prepared following the GeoMx-NGS Slide Preparation User Manual (MAN-10115-05) as per the RNA FFPE Manual Slide Preparation Protocol section in the user manual. Briefly, slides were deparaffinized using xylene, subjected to antigen retrieval, digested with proteinase K, hybridized overnight with the Human Whole Transcriptome Atlas probe set (catalog number 121401102), encompassing over 18,000 gene targets, and stained with morphology markers (pan-cytokeratin, SMA, and Syto83). The hybridized and stained slides were loaded onto the GeoMx instrument as per the GeoMx-NGS DSP Instrument User Manual (SEV-00087-05). Collected ROIs aspirate was processed as per the GeoMx-NGS Readout Library Prep User Manual (MAN-10117-05). The next-generation sequencing library was sequenced on the Illumina NovaSeq 6000 platform, targeting 200 reads per μm^2.

FASTQ files were converted to DCC files using GeoMx NGS Pipeline software. Briefly, reads were aligned to the RTS-ID barcode list, and PCR duplications were removed and then converted to DCC files. GeoMx data were transformed into a Seurat object for analysis. Gene counts were Q3 normalized, considering all target values, and 3000 informative features were selected. Integration was then performed using the FindIntegrationAnchors and IntegrateData functions. The top 30 principal components with a resolution of 0.5 were used to identify cell clusters. The FindAllMarker function with default parameters was used to find marker genes for each cluster.

scRNA-seq

Generation of single-cell suspensions was performed as previously described (Gudjonsson et al, 2020). Briefly, samples were incubated in 5 U/ml Dispase (StemCell, catalog number 07913) at 37 °C for 45 minutes. The epidermis was peeled from the dermis, cut into fine pieces, and incubated in 0.25% trypsin-EDTA (Gibco, Life Technologies, catalog number 25200) with 50 μg/ml DNase I (Thermo Fisher Scientific, catalog number DN25-100M) for 45 minutes at 37 °C, quenched with fetal bovine serum, and passed through a 70-μM cell strainer. Dermis was minced and digested in 0.1% collagenase II (Life Technologies, catalog number 17101-015) and 0.1% collagenase V (Sigma, catalog number C9263) in RPMI 1640 with 50 μg/ml DNase I for 90 minutes at 37 °C and strained through a 70-μM cell strainer. Dead cell removal was performed using a Dead Cell Removal Kit (Miltenyi Biotec).Epidermal and dermal cells were

then recombined and washed in PBS containing 0.04% BSA and resuspended at a concentration of approximately 1000 cells/μl.

Library generation was performed following the 10x Genomics Chromium Single Cell 3' v3.1 Reagents Kit (per the CG000315 Rev E. user guide), where we targeted 10,000 cells per sample for capture. Additional reagents included nuclease-free water (Thermo Fisher Scientific, AM9937), low Tris-EDTA buffer (Thermo Fisher Scientific, 12090-015), ethanol (Millipore Sigma, E7023-500ML), SPRIselect Reagent Kit (Beckman Coulter, B23318), 10% Tween 20 (Bio-Rad Laboratories, 1662404), glycerin (Ricca Chemical Company, 3290-32), and Qiagen Buffer EB (Qiagen, 19086). Each library was sequenced on the Illumina NovaSeq 6000 platform to target an average of approximately 50,000 reads per cell.

FASTQ files were aligned utilizing 10x Genomics Cloud Cell Ranger Count v7.1.0. Each library was aligned to an indexed Human GRCh38 genome. Preliminary analysis and visualization of the single-cell datasets were performed using the Seurat R package (version 4.3.1). Low-quality and dead cells (nGenes < 500 or > 6000 or percent mitochondria $> 10\%$) were excluded from the analysis. After SCTransform normalization of each patient dataset, 3000 informative features were selected, and all 8 datasets were integrated using the FindIntegrationAnchors function. This was followed by principal component analysis, generation of an Elbow Plot, and uniform manifold approximation and projection analysis using the first 20 principal components, RunUMAP, and FindNeighbors. Doublets were removed in 2 steps. All cells were first clustered with a low resolution (R) of 0.2 to remove large doublet clusters. Clustering at a high R of 6 was then performed, resulting in numerous small clusters that enabled the maximal removal of doublets. Subsequent analysis used an R of 0.3.

For subclustering analysis, we computationally isolated all cell clusters that expressed *PDGFRA* for fibroblasts, *PTPRC* for immune cells, and keratin markers *K5* and *K1* for keratinocytes from the integrated master dataset (Figure 3b). Downstream subclustering analysis was performed using R of 0.1 for fibroblasts, 0.25 for immune cells, and 0.16 for keratinocytes, using principal component of 20 for all.

Cell–cell communication and RNA velocity analyses

For cell–cell communication predictions, CellChat analysis was performed for each condition of the log-normalized integrated data for all patients or pair-wise data for each individual patient. The default parameter settings were adopted except that the ligand–receptor interaction database was set to be "Secreted Signaling." A total of 20 cell clusters were used for analysis, including 6 keratinocyte clusters (BSC, BC, SC1, SC2, GC, and cycling BCs), 7 immune cell clusters (CD4T1, CD4T2, CD8T1, CD8T2, cycTC, DCs/macrophages, and mast cells), 3 fibroblast clusters (FB1, FB2, and FB3), smooth muscle cells, pericytes, endothelial cells, and melanocytes.

Three methods, TFvelo, scVelo, and nlvelo, were used for RNA velocity analysis on keratinocytes under each condition, using default parameter settings. Both scVelo and nlvelo require the spliced and unspliced RNA counts, with scVelo modeling the splicing dynamics using linear equations and nlvelo using nonlinear equations (Haensel et al, 2020). TFvelo estimates transcriptional-regulation–driven RNA velocity by modeling the dynamics of target genes and their transcription factors, solely on the basis of the single-cell RNA counts without relying on splicing information (Li et al, 2024). For scVelo and nlvelo, loom files that contain the spliced and unspliced RNA counts were generated using the velocyto package (version 0.17). For nlvelo and TFvelo, 1000 cells from each condition were randomly sampled for analysis to save time.

Gene scoring, GO, and PROGENy analyses

Gene scoring analysis was performed in the AddModuleScore function using appropriate gene lists as previously described (Haensel et al, 2020).

GO enrichment for biological processes was done by selecting the markers ($-0.5 \geq \log_2$ fold change ≥ 0.5, adjusted $P < .05$) identified in 'FindMarkers' and executing the 'enrichGO' function of 'clusterProfiler' (version 4.8.3) on that dataset using the 'org. Hs.eg. db' database. The GO terms were presented by plot using ggplot2 (version 3.4.4). GO terms with a $P < .05$ were considered significantly enriched. Analysis of fibroblast and immune cell datasets was done after removing keratinocyte-specific genes from the DEG lists (Supplementary Tables S5 and S6).

Pathway activity scores were calculated using the 'progeny' function (organism = "Human", top = 100) from 'PROGENy' (version 1.22.0).

Keratinocyte culture and siRNA transfection

N/TERT-2G human keratinocytes were kindly provided by Jos P. H. Smits (Radboud University Medical Center, Nijmegen, The Netherlands), with permission from James Rheinwald (Harvard Medical School) (Dickson et al, 2000).

Stealth duplex siRNAs targeting *APOE* (gene bank identification NM_001302691.2) and *CXCL14* (gene bank identification NM_004887.5) were designed using Invitrogen BLOCK-iT RNAi Designer and were synthesized commercially (Thermo Fisher Scientific). Sequences of all the siRNAs are listed in Supplementary Table S7. A stealth negative control siRNA with 48% guanine and cytosine content (Thermo Fisher Scientific) was used as a scrambled control.

For siRNA knockdown, N/TERT-2G keratinocytes were plated on 6-well plates (Falcon, 40,000 cells per well) or 24-well plates (Falcon, 15,000 cells per well) in Keratinocyte SFM (1X) medium (Gibco) and were cultured at 37 °C with 95% air/5% carbon dioxide. At 40–50% confluency, cells were transfected with 100 pmol/well (6-well plate) or 20 pmol/well (24-well plate) of APOE siRNA, CXCL14 siRNA, or negative control siRNA, using 5 μl/well (6-well plate) or 1 μl/well (24-well plate) of Lipofectamine 2000 transfection reagent (Thermo Fisher Scientific), following the manufacturer's instructions. Six hours later, the medium was replaced with Keratinocyte SFM (1X) medium supplemented with penicillin–streptomycin (Gibco, 100 units/ml). Cells were harvested at 0, 24, 48, and 72 hours after transfection for proliferation analysis or at 48 hours for RT-qPCR or for use in 3-dimensional skin equivalent organotypic culture.

Proliferation analysis was performed on the basis of the method of McFarland laboratory (McFarland, 1995). Plates (24-well) of keratinocytes were frozen overnight at −80 °C and thawed at room temperature for 15 minutes. After trypsinization with 200 μl/well of 0.05% trypsin-EDTA (Gibco) in TNE buffer (10 mM Tris, 2 M sodium chloride, and 1 mM EDTA) at room temperature for 7 minutes, the plates were frozen thawed 1 more time. A total of 1.8 ml of 0.2% Hoechst 33258 (Thermo Fisher Scientific) in TNE buffer was added to each well, and the plates were gently agitated for 2 hours at room temperature. Hoechst 33258 intensity was measured using a Varioskan LUX multimode microplate reader (Thermo Fisher Scientific) with an excitation wavelength of 355 nm and an emission wavelength of 460 nm. A standard curve was constructed using double-stranded calf thymus DNA (Sigma-Aldrich) to determine the

sample DNA concentration. The proliferation analysis was repeated in 3 independent cultures with 4 replicate wells per treatment per culture.

RT-qPCR and bulk RNA sequencing

Total RNAs were isolated using the Quick-RNA Miniprep Kit (Zymo Research), following the manufacturer's instructions. Equal amounts of RNA from each treatment group were reverse transcribed into cDNA using the High-Capacity cDNA Reverse Transcription Kit (Applied Biosystems). RT-qPCR was conducted on a CFX96 Real-Time PCR Detection System (Bio-Rad Laboratories) using iTaq Universal SYBR Green Supermix (Bio-Rad Laboratories). Comparative analysis was performed using the ΔΔCt method to compare the expression of target genes with that of the housekeeping gene *GAPDH*. The sequences of all RT-qPCR primers are provided in Supplementary Table S7.

Total RNAs were sent to Novogene (Sacramento, CA) for bulk RNA-sequencing analysis. Briefly, mRNA was purified from total RNA using poly T oligo-attached magnetic beads. After fragmentation, the cDNA was synthesized using random hexamer primers. The library was checked with Qubit and real-time PCR for quantification and bioanalyzer for size distribution detection. Quantified libraries were pooled and sequenced on Illumina platforms. Raw data were processed to remove reads containing adapters and remove reads containing poly-N (>10% uncertain nucleotides) and low-quality reads (>50% of the bases with quality score < 5). All the downstream analyses were based on these high-quality clean data. Reference genome (hg38) and gene model annotation files were downloaded from the UCSC genome database. An index of the reference genome was built using Hisat2 (Mortazavi et al, 2008) (version 2.0.5), and paired-end reads were aligned to the reference genome using Hisat2 (version 2.0.5). featureCounts (Liao et al, 2014) (version 1.5.0-p)3 was used to count the reads numbers mapped to each gene. FPKM (Fragments Per Kilobase of transcript sequence per Millions base pairs) values for each gene were calculated on the basis of the length of the gene and the read count mapped to it. Differential expression (Anders and Huber, 2010) analysis of the 2 pairs of comparisons (NC vs *APOE* KD and NC vs *CXCL14* KD), each with 3 biological replicates, was performed using the DESeq2 package (1.20.0) in R (4.0.0). The *P*-values were adjusted using the Benjamini and Hochberg's approach for controlling the false discovery rate. Genes with an adjusted $P \leq .05$ were considered differentially expressed. GO enrichment analysis of DEGs was implemented by the clusterProfiler (4.6.0) R package. GO terms with corrected $P < .05$ were considered significantly enriched.

Human skin equivalent organotypic culture

Split-thickness human skin was purchased from the New York Firefighters Skin Bank. Devitalized de-epidermal dermis (DED) was prepared following the protocol by Li and Sen (2015). The DED was cut into 1.5 × 1.5 cm pieces, washed twice in complete DMEM (DMEM supplemented with 10% fetal bovine serum and 100 units/ml penicillin–streptomycin), and incubated in complete DMEM at 37 °C overnight before use. For the assembly of organotypic tissue, the cut DED was stretched in a 12-well plate, ensuring that the basement membrane was oriented downward and attached to the well bottom. Human primary dermal fibroblasts were isolated from discarded neonatal foreskin, as described previously by Lutz-Bonengel et al (2021) and maintained in complete DMEM. The primary fibroblasts (7.5×10^5) were seeded on top of the DED in 1.5 ml of complete DMEM, and the resulting cultures were incubated at 37 °C for 2 days. Subsequently, the fibroblast-containing DED was inverted and transferred to a new well of a 12-well plate with the basement membrane facing up. The culture medium was switched to Keratinocyte SFM, and N/TERT-2G cells (7.5×10^5) were seeded onto the basement membrane side in a total volume of 1.5 ml. After 2 days, the DED culture was moved into the upper chamber of a 40-μm cell strainer placed within a 6-well tissue culture plate filled with 4 ml of 3dGRO differentiation medium (Millipore Sigma), allowing the basement membrane side to be exposed to air. Differentiation medium was changed every other day, and organotypic tissue was harvested after 14 days, freshly frozen in optimal cutting temperature embedding compound on dry ice, and stored at −80 °C until use.

ETHICS STATEMENT

This study was approved by the Institutional Review Board of the University of California, Irvine (institutional review board number 1230). Written informed consent was obtained from all participants prior to enrollment, and records of informed consent have been retained in accordance with institutional policies.

DATA AVAILABILITY STATEMENT

The sequencing data reported in this work have been deposited in the Gene Expression Omnibus database under accession GSE274837 (single-cell RNA sequencing) (https://www.ncbi.nlm.nih.gov/geo/query/acc.cgi?acc=GSE274837) and GSE274068 (RNA sequencing) (https://www.ncbi.nlm.nih.gov/geo/query/acc.cgi?acc=GSE274068). Information required to reanalyze the data reported in this paper is available from the lead contact upon request.

ORCID

Xing Dai: http://orcid.org/0000-0001-8134-1365

CONFLICT OF INTEREST

CK has disclosed a previous or current relevant financial relationship or conflict of interest with the following companies: consultant of LEO Pharmaceuticals and Nuvig Therapeutics and an investigator for Incyte. The remaining authors state no conflict of interest.

ACKNOWLEDGMENTS

We thank the Genomics Research and Technology Hub at the University of California, Irvine for expert service. This work was supported by University of California, Irvine institutional seed grants from Institute for Precision Health, Skin Biology Resource-Based Center (P30-AR075047), Office of Research. Research personnel were partially supported by National Institute of Health Grants R35 GM145307 (XD), U01-AR073159 (QN, XD), National Science Foundation Grants DMS1763272 (QN, XD), CBET-2134916 (SXA), and Simons Foundation Grant 594598 (QN, XD).. CK is supported by a Dermatology Foundation Career Development Award. JX was supported by the California Institute of Regenerative Medicine Training Grant (EDUC4-12822). SS was supported by the National Institutes of Health T32 Interdisciplinary Training Program in Skin Biology (AR080622). Author order among cofirst authors was established through joint discussion with the senior author, reflecting the scope and nature of each author's contributions.

AUTHOR CONTRIBUTIONS

Conceptualization: CNK, XD; Data Curation: PS, QNg; Formal Analysis: PS, WZ; Funding Acquisition: CNK, XD; Investigation: PS, CNK, JX, SS, YJ, AN, JS, AE; Project Administration: XD; Resources: XD, BS, SXA, MO, QNe, RT; Supervision: XD; Validation: PS, JX; Visualization: PS, CNK, WZ, JX, SS, XD; Writing - Original Draft Preparation: PS, CNK, XD; Writing - Review and Editing: PS, CNK, WZ, JX, SS, QNg, YJ, AN, MO, RT, JS, BS, AE, SXA, QNe, XD

Disclaimer

The content is solely the responsibility of the authors and does not necessarily represent the official views of the California Institute for Regenerative Medicine.

REFERENCES

Akhmetshina A, Palumbo K, Dees C, Bergmann C, Venalis P, Zerr P, et al. Activation of canonical Wnt signalling is required for TGF-β-mediated fibrosis. Nat Commun 2012;3:735.

Anders S, Huber W. Differential expression analysis for sequence count data. Genome Biol 2010;11:R106.

Arnette CR, Roth-Carter QR, Koetsier JL, Broussard JA, Burks HE, Cheng K, et al. Keratinocyte cadherin desmoglein 1 controls melanocyte behavior through paracrine signaling. Pigment Cell Melanoma Res 2020;33:305–17.

Athota K, Kolalapudi SA. Vulvar lichen sclerosus in children: a prospective study over a 3 year period. Indian J Paediatr Dermatol 2021;22:131–5.

Bai L, Kong M, Duan Z, Liu S, Zheng S, Chen Y. M2-like macrophages exert hepatoprotection in acute-on-chronic liver failure through inhibiting necroptosis-S100A9-necroinflammation axis. Cell Death Dis 2021;12:93.

Beer HD, Longaker MT, Werner S. Reduced expression of PDGF and PDGF receptors during impaired wound healing. J Invest Dermatol 1997;109:132–8.

Bleeker MC, Visser PJ, Overbeek LI, Van Beurden M, Berkhof J. Lichen sclerosus: incidence and risk of vulvar squamous cell carcinoma. Cancer Epidemiol Biomarkers Prev 2016;25:1224–30.

Bose A, Teh MT, Mackenzie IC, Waseem A. Keratin K15 as a biomarker of epidermal stem cells. Int J Mol Sci 2013;14:19385–98.

Bradbury P, Nader CP, Cidem A, Rutting S, Sylvester D, He P, et al. Tropomyosin 2.1 collaborates with fibronectin to promote TGF-β1-induced contraction of human lung fibroblasts. Respir Res 2021;22:129.

Bradford J, Fischer G. Long-term management of vulval lichen sclerosus in adult women. Aust N Z J Obstet Gynaecol 2010;50:148–52.

Bunker CB. Occlusion, urine and genital lichen sclerosus. Indian J Dermatol Venereol Leprol 2012;78:367–8.

Chen J, Zhang Y, Tan W, Gao H, Xiao S, Gao J, et al. Silencing of long noncoding RNA NEAT1 improves Treg/Th17 imbalance in preeclampsia via the miR-485-5p/AIM2 axis. Bioengineered 2021;12:8768–77.

Chiang CC, Cheng WJ, Korinek M, Lin CY, Hwang TL. Neutrophils in psoriasis. Front Immunol 2019;10:2376.

Cohen E, Johnson CN, Wasikowski R, Billi AC, Tsoi LC, Kahlenberg JM, et al. Significance of stress keratin expression in normal and diseased epithelia. iScience 2024;27:108805.

Crowl JT, Heeg M, Ferry A, Milner JJ, Omilusik KD, Toma C, et al. Tissue-resident memory CD8+ T cells possess unique transcriptional, epigenetic and functional adaptations to different tissue environments. Nat Immunol 2022;23:1121–31.

Davila ML, Xu M, Huang C, Gaddes ER, Winter L, Cantorna MT, et al. CCL27 is a crucial regulator of immune homeostasis of the skin and mucosal tissues. iScience 2022;25:104426.

Day T, Selim MA, Allbritton JI, Scurry J, ISSVD Difficult Pathologic Diagnoses Committee (DPDC). Nonsclerotic lichen sclerosus: definition of a concept and pathologic description. J Low Genit Tract Dis 2023;27:358–64.

de Carvalho GC, Domingues R, de Sousa Nogueira MA, Calvielli Castelo Branco AC, Gomes Manfrere KC, Pereira NV, et al. Up-regulation of proinflammatory genes and cytokines induced by S100A8 in CD8+ T cells in Lichen Planus. Acta Derm Venereol 2015;96:485–9.

De Luca DA, Papara C, Vorobyev A, Staiger H, Bieber K, Thaçi D, et al. Lichen sclerosus: the 2023 update. Front Med (Lausanne) 2023;10:1106318.

Deng CC, Hu YF, Zhu DH, Cheng Q, Gu JJ, Feng QL, et al. Single-cell RNA-seq reveals fibroblast heterogeneity and increased mesenchymal fibroblasts in human fibrotic skin diseases. Nat Commun 2021;12:3709.

Dickson MA, Hahn WC, Ino Y, Ronfard V, Wu JY, Weinberg RA, et al. Human keratinocytes that express hTERT and also bypass a p16(INK4a)-enforced mechanism that limits life span become immortal yet retain normal growth and differentiation characteristics. Mol Cell Biol 2000;20:1436–47.

Dragan M, Sun P, Chen Z, Ma X, Vu R, Shi Y, et al. Epidermis-intrinsic transcription factor Ovol1 coordinately regulates barrier maintenance and neutrophil accumulation in psoriasis-like inflammation. J Invest Dermatol 2022;142:583–93.e5.

Duan X, Liu X, Liu N, Huang Y, Jin Z, Zhang S, et al. Inhibition of keratinocyte necroptosis mediated by RIPK1/RIPK3/MLKL provides a protective effect against psoriatic inflammation. Cell Death Dis 2020;11:134.

El Agha E, Moiseenko A, Kheirollahi V, De Langhe S, Crnkovic S, Kwapiszewska G, et al. Two-way conversion between lipogenic and myogenic fibroblastic phenotypes marks the progression and resolution of lung fibrosis. Cell Stem Cell 2017;20:261–73.e3.

ENCODE Project Consortium. The ENCODE (ENCyclopedia of DNA elements) project. Science 2004;306:636–40.

Epanchintsev A, Rauschendorf MA, Costanzo F, Calmels N, Obringer C, Sarasin A, et al. Defective transcription of ATF3 responsive genes, a marker for Cockayne syndrome. Sci Rep 2020;10:1105.

Farrell AM, Dean D, Millard PR, Charnock FM, Wojnarowska F. Cytokine alterations in lichen sclerosus: an immunohistochemical study. Br J Dermatol 2006;155:931–40.

Farrell AM, Marren P, Dean D, Wojnarowska F. Lichen sclerosus: evidence that immunological changes occur at all levels of the skin. Br J Dermatol 1999;140:1087–92.

Franco HL, Casasnovas J, Rodríguez-Medina JR, Cadilla CL. Redundant or separate entities?–roles of Twist1 and Twist2 as molecular switches during gene transcription. Nucleic Acids Res 2011;39:1177–86.

Giroux M, Schmidt M, Descoteaux A. IFN-gamma-induced MHC Class II expression: transactivation of Class II transactivator promoter IV by IFN regulatory Factor-1 is regulated by protein kinase C-alpha. J Immunol 2003;171:4187–94.

Goldstein AT, Marinoff SC, Christopher K, Srodon M. Prevalence of vulvar lichen sclerosus in a general gynecology practice. J Reprod Med 2005;50:477–80.

González-Amaro R, Cortés JR, Sánchez-Madrid F, Martín P. Is CD69 an effective brake to control inflammatory diseases? Trends Mol Med 2013;19:625–32.

Green DS, Young HA, Valencia JC. Current prospects of type II interferon γ signaling and autoimmunity. J Biol Chem 2017;292:13925–33.

Gudjonsson JE, Tsoi LC, Ma F, Billi AC, van Straalen KR, Vossen ARJV, et al. Contribution of plasma cells and B cells to hidradenitis suppurativa pathogenesis. JCI Insight 2020;5:e139930.

Guerrero-Juarez CF, Dedhia PH, Jin S, Ruiz-Vega R, Ma D, Liu Y, et al. Single-cell analysis reveals fibroblast heterogeneity and myeloid-derived adipocyte progenitors in murine skin wounds. Nat Commun 2019;10:650.

Haensel D, Jin S, Sun P, Cinco R, Dragan M, Nguyen Q, et al. Defining epidermal basal cell states during skin homeostasis and wound healing using single-cell transcriptomics. Cell Rep 2020;30:3932–47.e6.

He H, Suryawanshi H, Morozov P, Gay-Mimbrera J, Del Duca E, Kim HJ, et al. Single-cell transcriptome analysis of human skin identifies novel fibroblast subpopulation and enrichment of immune subsets in atopic dermatitis. J Allergy Clin Immunol 2020;145:1615–28.

Hiebert PR, Boivin WA, Abraham T, Pazooki S, Zhao H, Granville DJ. Granzyme B contributes to extracellular matrix remodeling and skin aging in apolipoprotein E knockout mice. Exp Gerontol 2011;46:489–99.

Horita H, Wada K, Rivas MV, Hara E, Jarvis ED. The dusp1 immediate early gene is regulated by natural stimuli predominantly in sensory input neurons. J Comp Neurol 2010;518:2873–901.

Hsieh WL, Huang YH, Wang TM, Ming YC, Tsai CN, Pang JH. IFI27, a novel epidermal growth factor-stabilized protein, is functionally involved in proliferation and cell cycling of human epidermal keratinocytes. Cell Prolif 2015;48:187–97.

Hu CW, Kornblau SM, Slater JH, Qutub AA. Progeny clustering: a method to identify biological phenotypes. Sci Rep 2015;5:12894.

Hu X, Li J, Fu M, Zhao X, Wang W. The JAK/STAT signaling pathway: from bench to clinic. Signal Transduct Target Ther 2021;6:402.

Hui ST, Gong L, Swichkow C, Blencowe M, Kaminska D, Diamante G, et al. Role of matrix Gla protein in transforming growth factor-β signaling and nonalcoholic steatohepatitis in mice. Cell Mol Gastroenterol Hepatol 2023;16:943–60.

Ibrahim AM, Sabet S, El-Ghor AA, Kamel N, Anis SE, Morris JS, et al. Fibulin-2 is required for basement membrane integrity of mammary epithelium. Sci Rep 2018;8:14139.

Ihim SA, Abubakar SD, Zian Z, Sasaki T, Saffarioun M, Maleknia S, et al. Interleukin-18 cytokine in immunity, inflammation, and autoimmunity: biological role in induction, regulation, and treatment. Front Immunol 2022;13:919973.

Iwayama T, Olson LE. Involvement of PDGF in fibrosis and scleroderma: recent insights from animal models and potential therapeutic opportunities. Curr Rheumatol Rep 2013;15:304.

Jiang Y, Tsoi LC, Billi AC, Ward NL, Harms PW, Zeng C, et al. Cytokinocytes: the diverse contribution of keratinocytes to immune responses in skin. JCI Insight 2020;5:e142067.

Jin S, Guerrero-Juarez CF, Zhang L, Chang I, Ramos R, Kuan CH, et al. Inference and analysis of cell-cell communication using CellChat. Nat Commun 2021;12:1088.

Jones RW, Scurry J, Neill S, MacLean AB. Guidelines for the follow-up of women with vulvar lichen sclerosus in specialist clinics. Am J Obstet Gynecol 2008;198:496.e1–3.

Junankar S, Baker LA, Roden DL, Nair R, Elsworth B, Gallego-Ortega D, et al. ID4 controls mammary stem cells and marks breast cancers with a stem cell-like phenotype. Nat Commun 2015;6:6548.

Kamaid A, Giráldez F. Btg1 and Btg2 gene expression during early chick development. Dev Dyn 2008;237:2158–69.

Kamata M, Tada Y. Dendritic cells and macrophages in the pathogenesis of psoriasis. Front Immunol 2022;13:941071.

Khan Mohammad Beigi P. The immunogenetics of morphea and lichen sclerosus. Adv Exp Med Biol 2022;1367:155–72.

Komatsu N, Saijoh K, Kuk C, Shirasaki F, Takehara K, Diamandis EP. Aberrant human tissue kallikrein levels in the stratum corneum and serum of patients with psoriasis: dependence on phenotype, severity and therapy. Br J Dermatol 2007;156:875–83.

Koumas L, Smith TJ, Feldon S, Blumberg N, Phipps RP. Thy-1 expression in human fibroblast subsets defines myofibroblastic or Lipofibroblastic phenotypes. Am J Pathol 2003;163:1291–300.

Kreuter A, Kryvosheyeva Y, Terras S, Moritz R, Möllenhoff K, Altmeyer P, et al. Association of autoimmune diseases with lichen sclerosus in 532 male and female patients. Acta Derm Venereol 2013;93:238–41.

Kurelic R, Krieg PF, Sonner JK, Bhaiyan G, Ramos GC, Frantz S, et al. Upregulation of phosphodiesterase 2A augments T cell activation by changing cGMP/cAMP cross-talk. Front Pharmacol 2021;12:748798.

Kyjacova L, Saup R, Rönsch K, Wallbaum S, Dukowic-Schulze S, Foss A, et al. IER2-induced senescence drives melanoma invasion through osteopontin. Oncogene 2021;40:6494–512.

La Manno G, Soldatov R, Zeisel A, Braun E, Hochgerner H, Petukhov V, et al. RNA velocity of single cells. Nature 2018;560:494–8.

Latinkic BV, O'Brien TP, Lau LF. Promoter function and structure of the growth factor-inducible immediate early gene cyr61. Nucleic Acids Res 1991;19:3261–7.

Lauffer F, Jargosch M, Krause L, Garzorz-Stark N, Franz R, Roenneberg S, et al. Type I immune response induces keratinocyte necroptosis and is associated with interface dermatitis. J Invest Dermatol 2018;138:1785–94.

LeBleu VS, Teng Y, O'Connell JT, Charytan D, Müller GA, Müller CA, et al. Identification of human epididymis protein-4 as a fibroblast-derived mediator of fibrosis. Nat Med 2013;19:227–31.

Lee A, Bradford J, Fischer G. Long-term management of adult vulvar lichen sclerosus: a prospective cohort study of 507 women. JAMA Dermatol 2015;151:1061–7.

Li J, Pan X, Yuan Y, Shen HB. TFvelo: gene regulation inspired RNA velocity estimation. Nat Commun 2024;15:1387.

Li J, Sen GL. Generation of genetically modified organotypic skin cultures using devitalized human dermis. J Vis Exp 2015;106:e53280.

Liao Y, Smyth GK, Shi W. featureCounts: an efficient general purpose program for assigning sequence reads to genomic features. Bioinformatics 2014;30:923–30.

Lin JY, Fisher DE. Melanocyte biology and skin pigmentation. Nature 2007;445:843–50.

Liso A, Venuto S, Coda ARD, Giallongo C, Palumbo GA, Tibullo D. IGFBP-6: at the crossroads of immunity, tissue repair and fibrosis. Int J Mol Sci 2022;23:4358.

Lloyd SM, Leon DB, Brady MO, Rodriguez D, McReynolds MP, Kweon J, et al. CDK9 activity switch associated with AFF1 and HEXIM1 controls differentiation initiation from epidermal progenitors. Nat Commun 2022;13:4408.

Loetscher P, Uguccioni M, Bordoli L, Baggiolini M, Moser B, Chizzolini C, et al. CCR5 is characteristic of Th1 lymphocytes. Nature 1998;391:344–5.

Lutz-Bonengel S, Niederstätter H, Naue J, Koziel R, Yang F, Sänger T, et al. Evidence for multi-copy Mega-NUMTs in the human genome. Nucleic Acids Res 2021;49:1517–31.

Ma F, Plazyo O, Billi AC, Tsoi LC, Xing X, Wasikowski R, et al. Single cell and spatial sequencing define processes by which keratinocytes and fibroblasts amplify inflammatory responses in psoriasis. Nat Commun 2023;14:3455.

Ma H, Feng PH, Yu SN, Lu ZH, Yu Q, Chen J. Identification and validation of TNFRSF4 as a high-profile biomarker for prognosis and immunomodulation in endometrial carcinoma [published correction appears in BMC Cancer 2022;22:592]. BMC Cancer 2022;22:543.

Machado L, Geara P, Camps J, Dos Santos M, Teixeira-Clerc F, Van Herck J, et al. Tissue damage induces a conserved stress response that initiates quiescent muscle stem cell activation. Cell Stem Cell 2021;28:1125–35.e7.

Marangoni RG, Datta P, Paine A, Duemmel S, Nuzzo M, Sherwood L, et al. Thy-1 plays a pathogenic role and is a potential biomarker for skin fibrosis in scleroderma. JCI Insight 2022;7:e149426.

Martin P, Palmer G, Vigne S, Lamacchia C, Rodriguez E, Talabot-Ayer D, et al. Mouse neutrophils express the decoy type 2 interleukin-1 receptor (IL-1R2) constitutively and in acute inflammatory conditions. J Leukoc Biol 2013;94:791–802.

Martinez FO, Gordon S, Locati M, Mantovani A. Transcriptional profiling of the human monocyte-to-macrophage differentiation and polarization: new molecules and patterns of gene expression. J Immunol 2006;177:7303–11.

Martins Cardoso R, Creemers E, Absalah S, Gooris GS, Hoekstra M, Van Eck M, et al. Hypercholesterolemia in young adult APOE$^{-/-}$ mice alters epidermal lipid composition and impairs barrier function. Biochim Biophys Acta Mol Cell Biol Lipids 2019;1864:976–84.

McFarland DC, Pesall JE, Gilkerson KK, Ferrin NH. The response to growth factors of cultured satellite cells derived from turkeys having different growth rates. Cytobios 1995;82:229–38.

Melnick LE, Steuer AB, Bieber AK, Wong PW, Pomeranz MK. Lichen sclerosus among women in the United States. Int J Womens Dermatol 2020;6:260–2.

Merritt CR, Ong GT, Church SE, Barker K, Danaher P, Geiss G, et al. Multiplex digital spatial profiling of proteins and RNA in fixed tissue. Nat Biotechnol 2020;38:586–99.

Mori M, Nakajima M, Mikami Y, Seki S, Takigawa M, Kubo T, et al. Transcriptional regulation of the cartilage intermediate layer protein (CILP) gene. Biochem Biophys Res Commun 2006;341:121–7.

Mortazavi A, Williams BA, McCue K, Schaeffer L, Wold B. Mapping and quantifying mammalian transcriptomes by RNA-Seq. Nat Methods 2008;5:621–8.

Nguyen LT, Ohashi PS. Clinical blockade of PD1 and LAG3–potential mechanisms of action. Nat Rev Immunol 2015;15:45–56.

Otano I, Azpilikueta A, Glez-Vaz J, Alvarez M, Medina-Echeverz J, Cortés-Domínguez I, et al. CD137 (4-1BB) costimulation of CD8+ T cells is more potent when provided in cis than in trans with respect to CD3-TCR stimulation. Nat Commun 2021;12:7296.

Paulis G, Berardesca E. Lichen sclerosus: the role of oxidative stress in the pathogenesis of the disease and its possible transformation into carcinoma. Res Rep Urol 2019;11:223–32.

Philippeos C, Telerman SB, Oulès B, Pisco AO, Shaw TJ, Elgueta R, et al. Spatial and single-cell transcriptional profiling identifies functionally distinct human dermal fibroblast subpopulations. J Invest Dermatol 2018;138:811–25.

Pichler AC, Carrié N, Cuisinier M, Ghazali S, Voisin A, Pierre-Paul A, et al. TCR-independent CD137 (4-1BB) signaling promotes CD8^{+}-exhausted T cell proliferation and terminal differentiation. Immunity 2023;56:1631–48.e10.

Pilatz A, Altinkilic B, Schormann E, Maegel L, Izykowski N, Becker J, et al. Congenital phimosis in patients with and without lichen sclerosus: distinct expression patterns of tissue remodeling associated genes. J Urol 2013;189:268–74.

Platanias LC. Mechanisms of type-I- and type-II-interferon-mediated signalling. Nat Rev Immunol 2005;5:375–86.

Porter AG, Jänicke RU. Emerging roles of caspase-3 in apoptosis. Cell Death Differ 1999;6:99–104.

Rauschmayr T, Groves RW, Kupper TS. Keratinocyte expression of the type 2 interleukin 1 receptor mediates local and specific inhibition of interleukin 1-mediated inflammation. Proc Natl Acad Sci USA 1997;94:5814–9.

Ron A, Azeloglu EU, Calizo RC, Hu M, Bhattacharya S, Chen Y, et al. Cell shape information is transduced through tension-independent mechanisms. Nat Commun 2017;8:2145.

Ryan GE, Harris JE, Richmond JM. Resident Memory T Cells in autoimmune skin diseases. Front Immunol 2021;12:652191.

Safronova A, Araujo A, Camanzo ET, Moon TJ, Elliott MR, Beiting DP, et al. Alarmin S100A11 initiates a chemokine response to the human pathogen Toxoplasma gondii. Nat Immunol 2019;20:64–72.

Saito N, Qiao H, Yanagi T, Shinkuma S, Nishimura K, Suto A, et al. An annexin A1-FPR1 interaction contributes to necroptosis of keratinocytes in severe cutaneous adverse drug reactions. Sci Transl Med 2014;6:245ra95.

Schmit K, Chen J-W, Ayama-Canden S, Fransolet M, Finet L, Demazy C, et al. Characterization of the role of TMEM45A in cancer cell sensitivity to cisplatin. Cell Death Dis 2019;10:919.

Seliger B, Ruiz-Cabello F, Garrido F. IFN inducibility of major histocompatibility antigens in tumors. Adv Cancer Res 2008;101:249–76.

Shao S, Tsoi LC, Sarkar MK, Xing X, Xue K, Uppala R, et al. IFN-γ enhances cell-mediated cytotoxicity against keratinocytes via JAK2/STAT1 in lichen planus. Sci Transl Med 2019;11:eaav7561.

Shimomura Y, Agalliu D, Vonica A, Luria V, Wajid M, Baumer A, et al. APCDD1 is a novel Wnt inhibitor mutated in hereditary hypotrichosis simplex. Nature 2010;464:1043–7.

Shirley SH, von Maltzan K, Robbins PO, Kusewitt DF. Melanocyte and melanoma cell activation by calprotectin. J Skin Cancer 2014;2014:846249.

Sikder HA, Devlin MK, Dunlap S, Ryu B, Alani RM. Id proteins in cell growth and tumorigenesis. Cancer Cell 2003;3:525–30.

Smits J, Niehues H, Rikken G, van Vlijmen-Willems I, Zeeuwen P, Schalkwijk J, et al. 113 Immortalized N/TERT keratinocytes: an excellent and versatile alternative for primary keratinocytes in experimental dermatological research. J Invest Dermatol 2017;137:S212.

Solé-Boldo L, Raddatz G, Schütz S, Mallm JP, Rippe K, Lonsdorf AS, et al. Single-cell transcriptomes of the human skin reveal age-related loss of fibroblast priming. Commun Biol 2020;3:188.

Srikrishna G. S100A8 and S100A9: new insights into their roles in malignancy. J Innate Immun 2012;4:31–40.

Sun F, Liao M, Tao Z, Hu R, Qin J, Tao W, et al. Identification of panoptosis-related predictors for prognosis and tumor microenvironment by multiomics analysis in glioma. J Cancer 2024;15:2486–504.

Sun L, Wang H, Wang Z, He S, Chen S, Liao D, et al. Mixed lineage kinase domain-like protein mediates necrosis signaling downstream of RIP3 kinase. Cell 2012;148:213–27.

Szabo PA, Miron M, Farber DL. Location, location, location: tissue resident memory T cells in mice and humans. Sci Immunol 2019;4:eaas9673.

Tang Z, Tong X, Huang J, Liu L, Wang D, Yang S. Research progress of keratinocyte-programmed cell death in UV-induced Skin photodamage. Photodermatol Photoimmunol Photomed 2021;37:442–8.

Terlou A, Santegoets LA, Van Der Meijden WI, Heijmans-Antonissen C, Swagemakers SM, Van Der Spek PJ, et al. An autoimmune phenotype in vulvar lichen sclerosus and lichen planus: a Th1 response and high levels of microRNA-155. J Invest Dermatol 2012;132:658–66.

Tibbitt CA, Stark JM, Martens L, Ma J, Mold JE, Deswarte K, et al. Single-cell RNA sequencing of the T helper cell response to house dust mites defines a distinct gene expression signature in airway Th2 cells. Immunity 2019;51:169–84.e5.

Tong X, Burks HE, Ren Z, Koetsier JL, Roth-Carter QR, Green KJ. Crosstalk in skin: loss of desmoglein 1 in keratinocytes inhibits $BRAF^{V600E}$-induced Cellular senescence in human melanocytes. J Invest Dermatol 2025;145:1740–52.e4.

Tran DA, Tan X, Macri CJ, Goldstein AT, Fu SW. Lichen sclerosus: an autoimmunopathogenic and genomic enigma with emerging genetic and immune targets. Int J Biol Sci 2019;15:1429–39.

Trojanowska M. Role of PDGF in fibrotic diseases and systemic sclerosis. Rheumatology (Oxford) 2008;47:v2–4.

Tsujihana K, Tanegashima K, Santo Y, Yamada H, Akazawa S, Nakao R, et al. Circadian protection against bacterial skin infection by epidermal CXCL14-mediated innate immunity. Proc Natl Acad Sci USA 2022;119:e2116027119.

Tullai JW, Schaffer ME, Mullenbrock S, Sholder G, Kasif S, Cooper GM. Immediate-early and delayed primary response genes are distinct in function and genomic architecture. J Biol Chem 2007;282:23981–95.

van Drongelen V, Scavuzzi BM, Nogueira SV, Miller FW, Sawalha AH, Holoshitz J. HLA-DRB1 allelic epitopes that associate with autoimmune disease risk or protection activate reciprocal macrophage polarization. Sci Rep 2021;11:2599.

Vittrup G, Mørup L, Heilesen T, Jensen D, Westmark S, Melgaard D. Quality of life and sexuality in women with lichen sclerosus: a cross-sectional study. Clin Exp Dermatol 2022;47:343–50.

Vu R, Jin S, Sun P, Haensel D, Nguyen QH, Dragan M, et al. Wound healing in aged skin exhibits systems-level alterations in cellular composition and cell-cell communication. Cell Rep 2022;40:111155.

Wang H, Guo M, Wei H, Chen Y. Targeting p53 pathways: mechanisms, structures, and advances in therapy. Signal Transduct Target Ther 2023;8:92.

Wang L, Lv Q, Guo J, Wang J, Pan J. Transcriptome profiling and network analysis provide insights into the pathogenesis of vulvar lichen sclerosus. Front Genet 2022;13:905450.

Wang S, Drummond ML, Guerrero-Juarez CF, Tarapore E, MacLean AL, Stabell AR, et al. Single cell transcriptomics of human epidermis identifies basal stem cell transition states. Nat Commun 2020;11:4239.

Weyers W. Hypertrophic lichen sclerosus sine sclerosis: clues to histopathologic diagnosis when presenting as psoriasiform lichenoid dermatitis. J Cutan Pathol 2015;42:118–29.

Wiedemann J, Billi AC, Bocci F, Kashgari G, Xing E, Tsoi LC, et al. Differential cell composition and split epidermal differentiation in human palm, sole, and hip skin. Cell Rep 2023;42:111994.

Wijaya M, Lee G, Fischer G. Quality of life of women with untreated vulval lichen sclerosus assessed with vulval quality of life index (VQLI). Australas J Dermatol 2021;62:177–82.

Wijdeven RH, van Luijn MM, Wierenga-Wolf AF, Akkermans JJ, van den Elsen PJ, Hintzen RQ, et al. Chemical and genetic control of IFNγ-induced MHCII expression. EMBO Rep 2018;19:e45553.

Wölfl M, Kuball J, Eyrich M, Schlegel PG, Greenberg PD. Use of CD137 to study the full repertoire of CD8+ T cells without the need to know epitope specificities. Cytometry A 2008;73A:1043–9.

Yang X, Wang Z, Samovich SN, Kapralov AA, Amoscato AA, Tyurin VA, et al. PHLDA2-mediated phosphatidic acid peroxidation triggers a distinct ferroptotic response during tumor suppression. Cell Metab 2024;36:762–77.e9.

Yu H, Königshoff M, Jayachandran A, Handley D, Seeger W, Kaminski N, et al. Transgelin is a direct target of TGF-beta/Smad3-dependent epithelial cell migration in lung fibrosis. FASEB J 2008;22:1778–89.

Zhang L, Zhou F, ten Dijke P. Signaling interplay between transforming growth factor-β receptor and PI3K/AKT pathways in cancer. Trends Biochem Sci 2013;38:612–20.

Zhang P, Cao L, Zhou R, Yang X, Wu M. The lncRNA Neat1 promotes activation of inflammasomes in macrophages. Nat Commun 2019;10:1495.

Zhang X, Yin M, Zhang LJ. Keratin 6, 16 and 17-critical barrier alarmin molecules in skin wounds and psoriasis. Cells 2019;8:807.

Zhao Y, Zhao S, Li H, Qin X, Wu X. Expression of galectin-7 in vulvar lichen sclerosus and its effect on dermal fibroblasts. Oncol Lett 2018;16:2559–64.

Zou Z, Long X, Zhao Q, Zheng Y, Song M, Ma S, et al. A single-cell transcriptomic atlas of human skin aging. Dev Cell 2021;56:383–97.e8.

Zucker SN, Fink EE, Bagati A, Mannava S, Bianchi-Smiraglia A, Bogner PN, et al. Nrf2 amplifies oxidative stress via induction of Klf9. Mol Cell 2014;53:916–28.

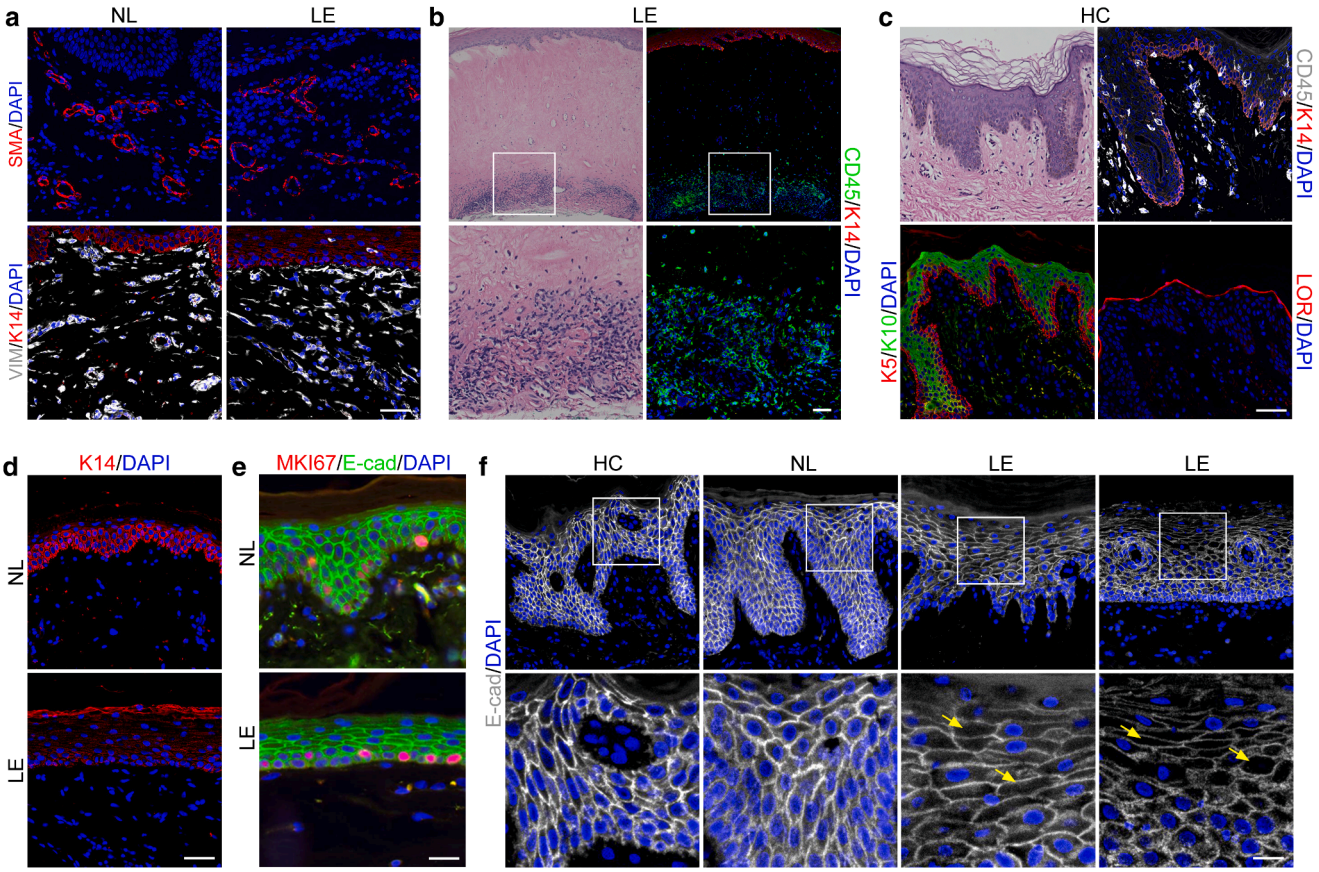

Supplementary Figure S1. Additional histologic and immunofluorescence analyses of control (HC and NL) and LE skin samples. This figure is related to Figure 1. (**a**) Immunofluorescence for SMA (top), vimentin, and K14 (bottom). Bar = 50 μm. (**b**) H&E (left) and CD45/K14 immunostaining (right) of a sclerotic LE sample with cellular aggregates deep in the reticular dermis. Bottom images represent a higher magnification of the boxed areas in top images. Bar = 100 μm and 27 μm in top and bottom panels, respectively. (**c**) H&E and immunostaining analysis of HC control. Bar = 50 μm. (**d**) LE sample from a patient with VLS shows altered K14 expression compared with matched NL sample (bottom). Bar = 50 μm. (**e**) Ki-67 and (**f**) E-cadherin immunostaining of HC, NL, and LE samples. Bottom images in **f** represent a higher magnification of the boxed areas in top images. Bar = 25 μm in **e** and 50 μm and 15 μm in top and bottom panels of **f**, respectively. HC, healthy control; K14, keratin 14; LE, lesional; NL, nonlesional; SMA, smooth muscle actin; VLS, vulvar lichen sclerosus.

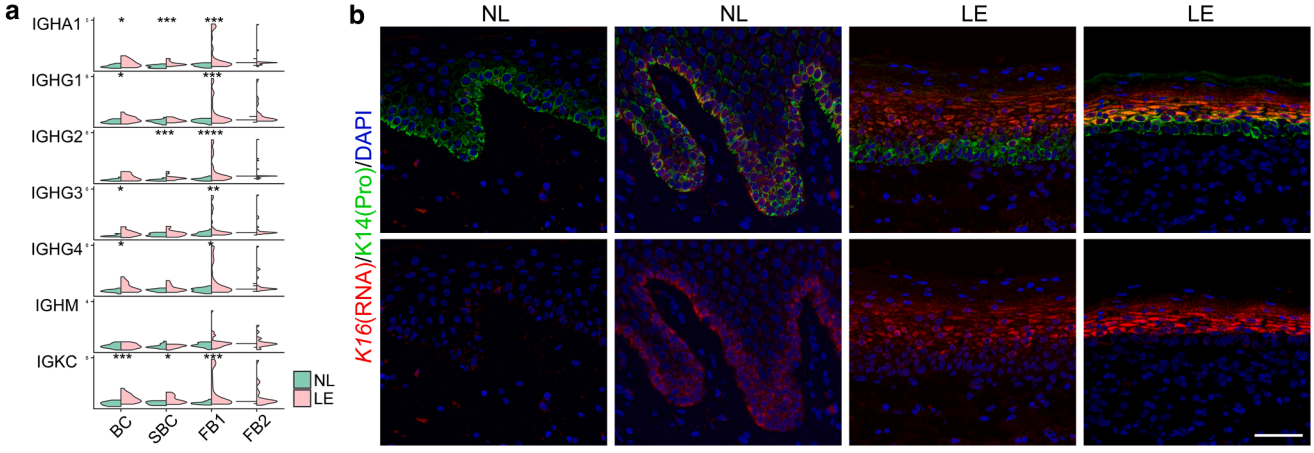

Supplementary Figure S2. GeoMx and RNAScope data revealing IgG and K16 expression in LE samples. This figure is related to Figure 2. (**a**) IgG gene expression by cluster in NL compared with that in LE skin by GeoMx analysis. BC denotes basal cells, SBC denotes suprabasal cells, and FB denotes fibroblasts. $^{*}P < .05$, $^{**}P < .01$, $^{***}P < .005$, $^{****}P < .001$. (**b**) RNAScope data showing spatial distribution of K16 transcripts along with K14 protein in LE compared with that in NL skin. Bar = 50 μm. K14, keratin 14; K16, keratin 16; LE, lesional; NL, nonlesional.

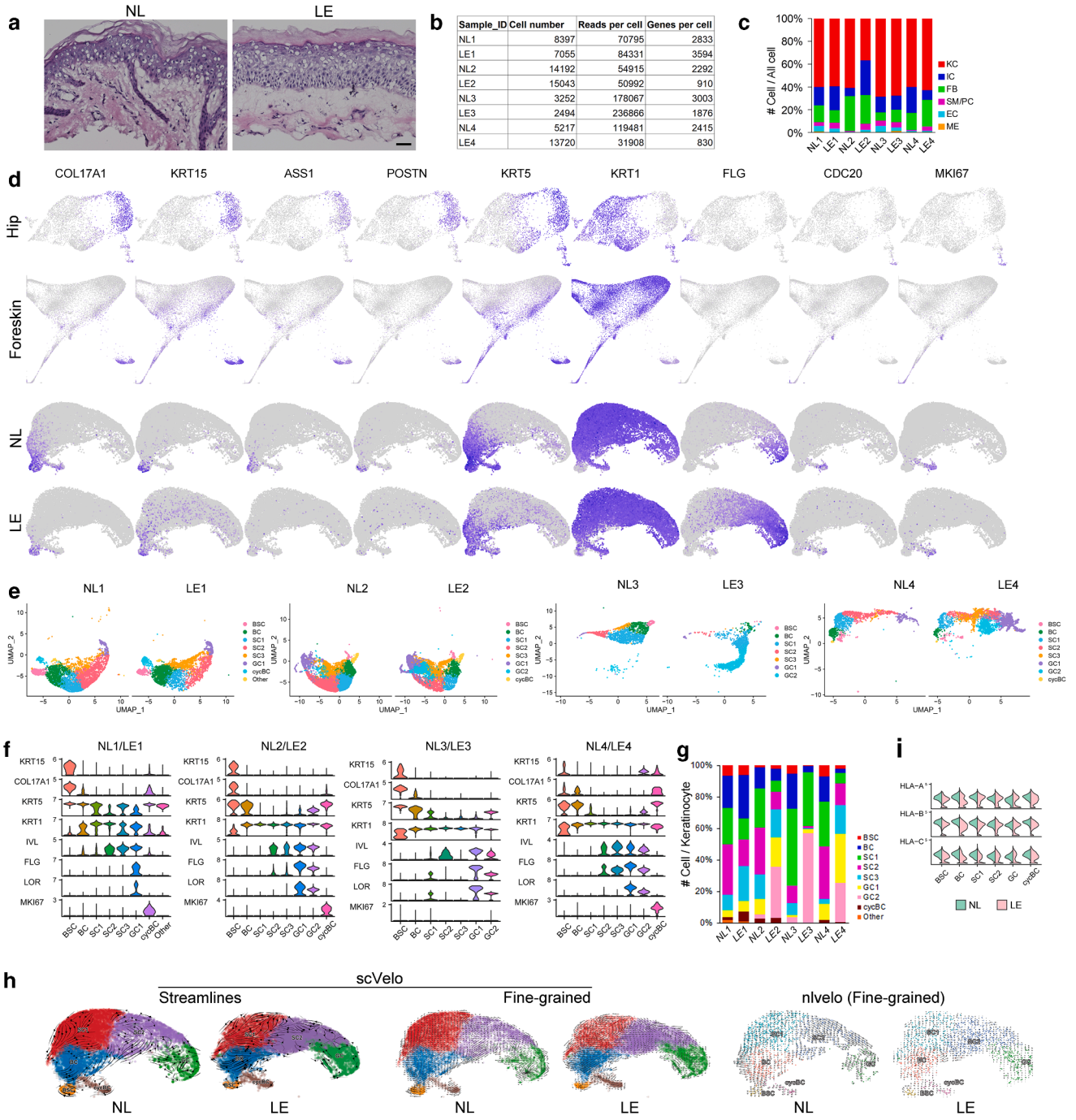

Supplementary Figure S3. Additional information for scRNA-seq, with pairwise analyses of keratinocyte subclusters from NL and LE samples per patient. This figure is related to Figure 3. (**a**) Histology of NL and LE skin from patient 5. Bar = 25 μm. (**b**) Table with number of captured cells per skin biopsy sample, average reads per cell, and genes per cell. (**c**) Bar plot showing relative proportions of each of the major cell types per patient and sample identities in the integrated dataset. KC denotes keratinocytes, IC denotes immune cells, FB denotes fibroblasts, SM/PC denotes smooth muscle cell/pericytes, EC denotes endothelial cells, and ME denotes melanocytes. (**d**) Feature plots of the indicated genes, including epidermal differentiation markers, in hip and foreskin in published data (top panels) and in integrated scRNA-seq data from vulvar keratinocytes in NL and LE skin (bottom panels). (**e**) UMAPs of keratinocyte subclusters using pairwise aggregation of patient-matched NL and LE samples without batch correction. (**f**) Violin plots of select markers for each subtype of keratinocytes using pairwise aggregation. (**g**) Bar plot showing relative proportions of each keratinocyte subcluster using pairwise aggregation. (**i**) Split violin plots of HLA-A/B/C expression in keratinocyte subclusters from the integrated data. (**h**) Projection of RNA velocity fields onto the UMAP space of keratinocytes in NL and LE from integrated data using 2 different methods: scVelo (streamlines, left 2 panels; fine grained, middle 2 panels) and nlvelo (fine grained, right 2 panels). LE, lesional; NL, nonlesional; scRNA-seq, single-cell RNA sequencing; UMAP, uniform manifold approximation and projection.

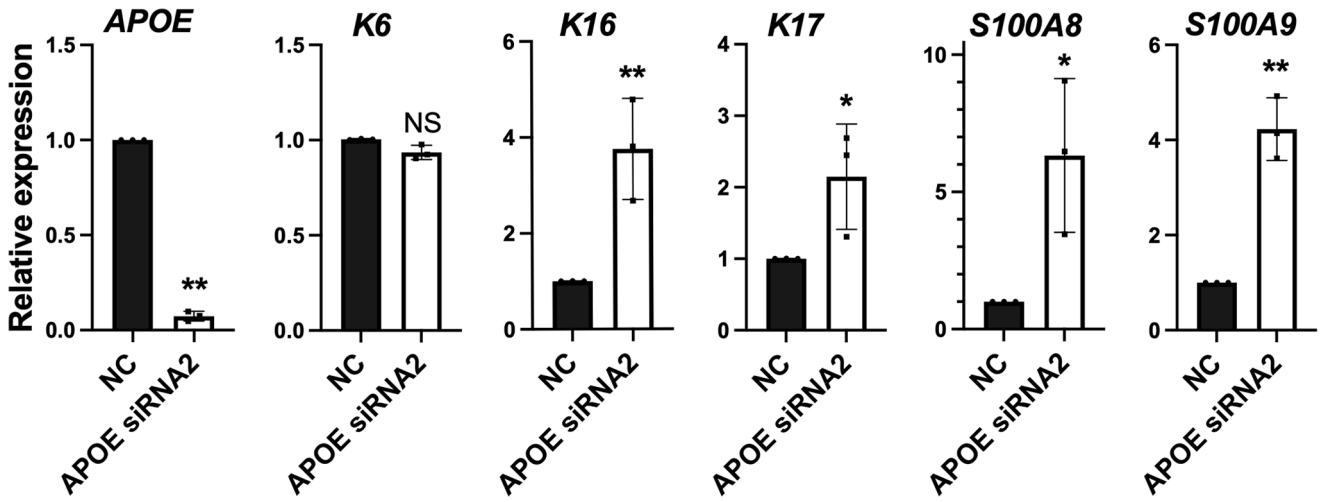

Supplementary Figure S4. RT-qPCR results of the indicated genes analyzed 48 h after transfection with APOE siRNA2. This figure is related to Figure 4. Note that 2 different siRNAs were used to minimize off-target effect. $^{**}P < .01$ and $^{*}P < .05$. h, hour; K16, keratin 16; K17, keratin 17; K6, keratin 6; ns, not significant; siRNA, small interfering RNA.

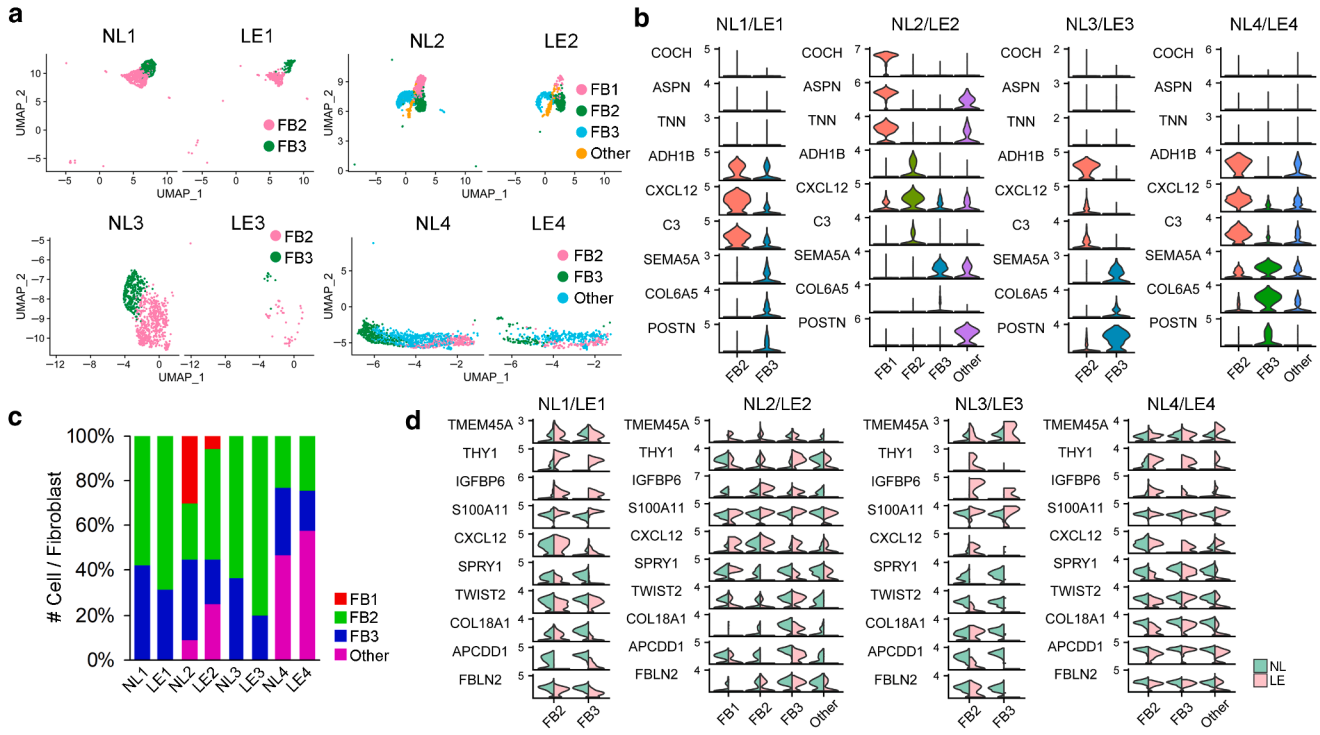

Supplementary Figure S5. Molecular alterations in LE fibroblasts. This figure is related to Figure 5. (**a**) UMAPs of fibroblast subclusters using pairwise aggregation of patient-matched NL and LE samples without batch correction. Patient 1 = NL1, LE1; Patient 2 = NL2, LE2; Patient 3 = NL3, LE3; Patient 4 = NL4, LE4. (**b**) Violin plots of marker genes for fibroblast subclusters in each patient. (**c**) Bar plot showing relative proportions of each fibroblast subcluster using pairwise aggregation. (**d**) Split violin plots of select top DEGs in fibroblast subclusters identified using pairwise aggregation. DEG, differentially expressed gene; LE, lesional; NL, nonlesional; UMAP, uniform manifold approximation and projection.

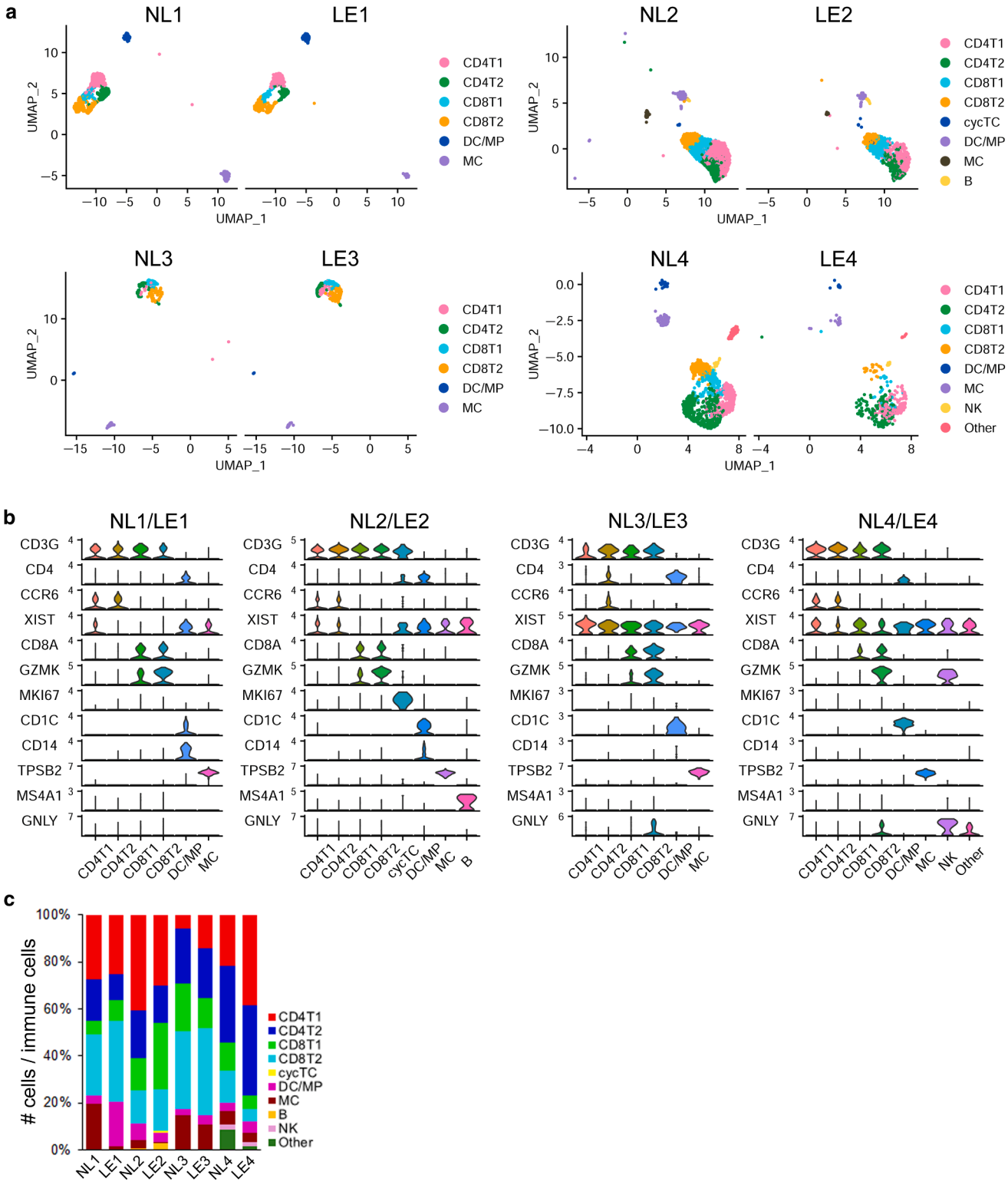

Supplementary Figure S6. Molecular alterations in LE immune cells. This figure is related to Figure 5. (**a**) UMAPs of immune cell subclusters using pairwise aggregation of patient-matched NL and LE samples without batch correction. (**b**) Violin plots of select markers for each subtype of immune cells using pairwise aggregation. (**c**) Bar plot showing relative proportions of each immune cell subcluster using pairwise aggregation. LE, lesional; NL, nonlesional; UMAP, uniform manifold approximation and projection.

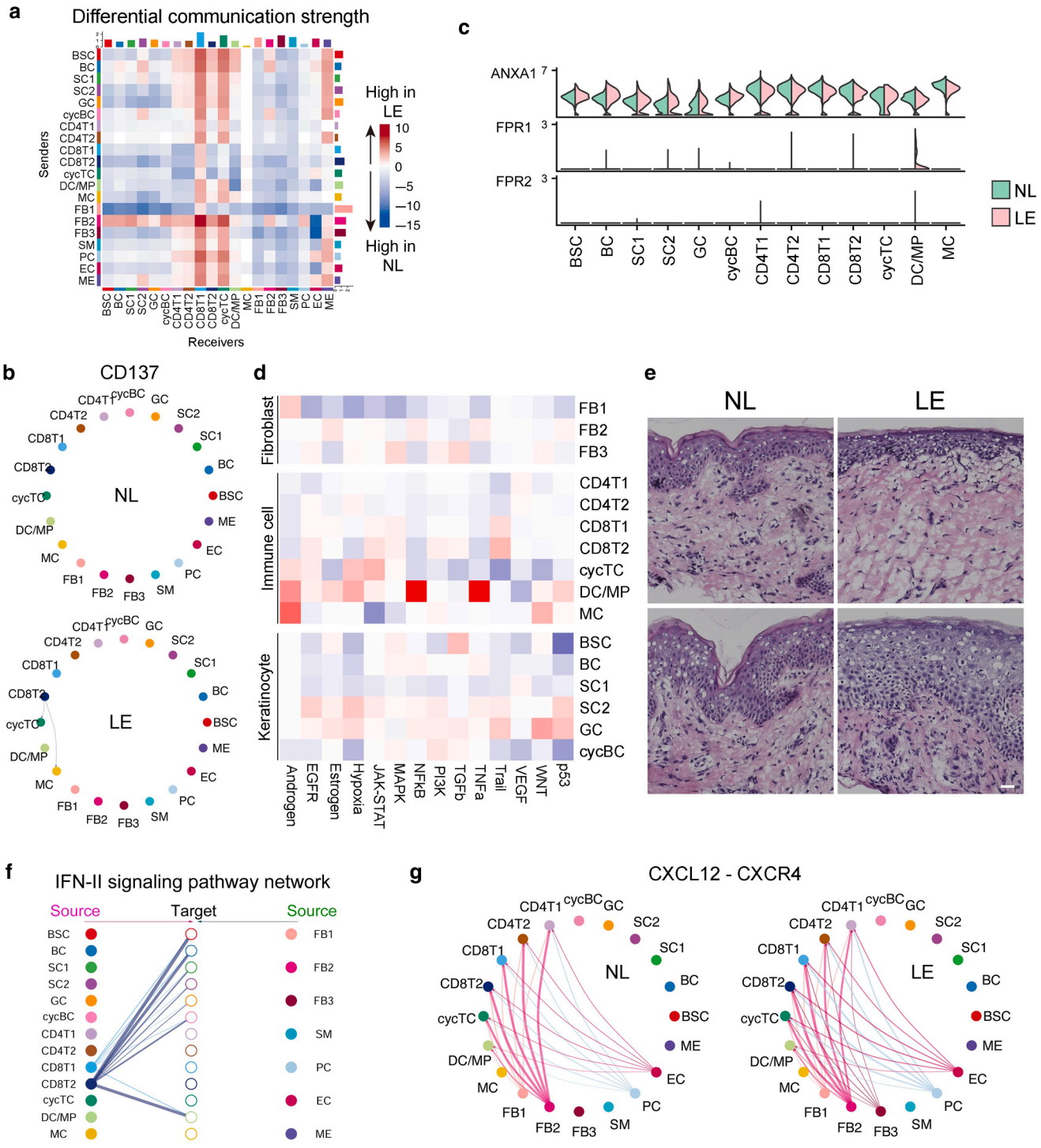

Supplementary Figure S7. Inferred alterations in signaling network and pathway activity in LE skin. This figure is related to Figure 6. (**a**) CellChat analysis after removal of most of the fibroblasts contaminated with keratinocyte transcripts, showing heatmap (by weight) summarizing differential communication strength between any 2 cell groups in LE compared with that in NL. See Figure 6b for comparison. (**B**) Chord diagrams of the inferred CD137 signaling network in NL versus LE skin. (**c**) Violin plots of expression of ANXA1 and its receptors, FRP1 and FRP2, in all keratinocyte and immune cell subclusters. (**d**) PROGENy analysis using scRNA-seq data of signaling pathway activation by cell type/subtype in fibroblasts, immune cells, and keratinocytes. (**e**) Histological images of 2 different regions of NL and LE skin from patient 4. Bar = 25 μm. (**f**) Hierarchy plots of IFN II signaling from all cells to keratinocytes and immune cells. (**g**) Chord diagrams of the inferred CXCL12–CXCR4 signaling network in NL versus LE skin. LE, lesional; NL, nonlesional; scRNA-seq, single-cell RNA sequencing.